

Cutting the Scotogenic loop: Adding flavor to Dark Matter

Ranjeet Kumar,^{1,*} Newton Nath,^{2,3,†} and Rahul Srivastava^{1,‡}

¹*Department of Physics, Indian Institute of Science Education and Research - Bhopal,
Bhopal Bypass Road, Bhauri, Bhopal 462066, India*

²*Instituto de Física Corpuscular, CSIC-Universitat de València,
and Departament de Física Teòrica, Universitat de València,
C/Catedrático José Beltrán 2, Paterna 46980, Spain*

³*Istituto Nazionale di Fisica Nucleare, Via Orabona 4, 70126 Bari, Italy*

We introduce a framework for hybrid neutrino mass generation, wherein scotogenic dark sector particles, including dark matter, are charged non-trivially under the A_4 flavor symmetry. The spontaneous breaking of the A_4 group to residual \mathbb{Z}_2 subgroup results in the “cutting” of the radiative loop. As a consequence the neutrinos acquire mass through the hybrid “scoto-seesaw” mass mechanism, combining aspects of both the tree-level seesaw and one-loop scotogenic mechanisms, with the residual \mathbb{Z}_2 subgroup ensuring the stability of the dark matter. The flavor symmetry also leads to several predictions including the normal ordering of neutrino masses and “generalized $\mu - \tau$ reflection symmetry” in leptonic mixing. Additionally, it gives testable predictions for neutrinoless double beta decay and a lower limit on the lightest neutrino mass. Finally, $A_4 \rightarrow \mathbb{Z}_2$ breaking also leaves its imprint on the dark sector and ties it with the neutrino masses and mixing. The model allows only scalar dark matter, whose mass has a theoretical upper limit of $\lesssim 600$ GeV, with viable parameter space satisfying all dark matter constraints, available only up to about 80 GeV. Conversely, fermionic dark matter is excluded due to constraints from the neutrino sector. Various aspects of this highly predictive framework can be tested in both current and upcoming neutrino and dark matter experiments.

1. INTRODUCTION

Despite its remarkable success in elucidating various observed natural phenomena, the Standard Model (SM) grapples with several unresolved questions. A notable limitation lies in its inability to explain the experimentally observed non-zero neutrino masses at a renormalizable level and their mixing patterns, as observed in solar and atmospheric neutrino oscillation experiments [1, 2]. There are several proposals in the literature to explain the tiny masses of neutrinos. Although these models provide an

* ranjeet20@iiserb.ac.in

† newton.nath@ific.uv.es

‡ rahul@iiserb.ac.in

understanding of the smallness of neutrino masses through various mass mechanisms, they do not shed light on the mixing and flavor structure of the leptonic sector. New flavor symmetries are often used to understand the leptonic (and/or quark) mixing structure. This flavor symmetry approach has proven highly successful in elucidating and predicting the flavor structure. Notably, the discrete non-abelian A_4 symmetry [3–5] has been the most popular flavor group used for such purpose. However, the flavor symmetric approach often fails to incorporate the existence of the two different mass scales namely, the atmospheric mass-squared difference, Δm_{atm}^2 , and the solar mass-squared difference, Δm_{sol}^2 , observed in neutrino oscillation experiments [6–8].

Apart from the neutrino sector, the absence of a viable candidate for cosmological dark matter (DM) in the SM raises another significant concern. DM is typically expected to be electrically neutral, non-baryonic particle(s), and the recent Planck data indicates that it constitutes approximately 85% of the observed matter in the Universe [9]. Thus, any beyond the SM (BSM) extension should address both these shortcomings. The “scotogenic” mechanism, originally proposed in [10], remains one of the

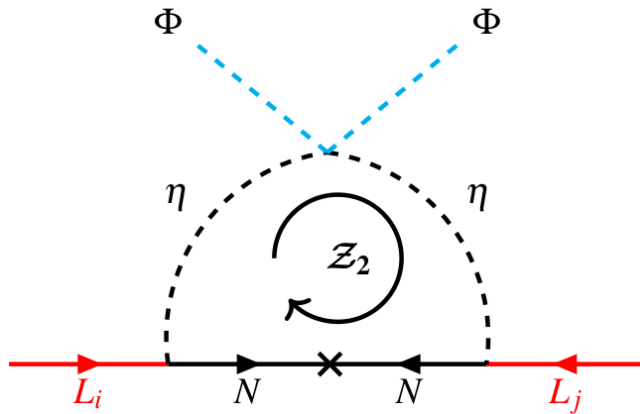


FIG. 1: Neutrino mass generation at the one-loop level in the canonical scotogenic model. Note that here a new dark Z_2 symmetry is needed to ensure DM stability.

simplest and most elegant approaches to establish a possible connection between the DM and neutrino mass generation. The hallmark of the scotogenic framework is the loop-level generation of neutrino masses through “dark sector” particles running in the loop as shown in Fig. 1, with the lightest dark sector particle being the DM. The scotogenic mechanism and its variants have received much attention in recent times [11–27]. However, it is worth pointing out here that the canonical scotogenic model [10] requires an *ad-hoc* Z_2 symmetry, as shown in Fig. 1, to ensure the stability of DM. The various variants of the scotogenic model known in the literature, also require a new symmetry to ensure the stability of the DM. Furthermore, like other neutrino mass mechanisms, it also fails to explain the flavor structure of the lepton sector or the presence of two different mass scales in neutrino oscillations.

Recently, in [28], an attempt has been made to successfully explain the origin of the two mass-

squared differences observed in neutrino oscillation data while preserving the main features of the scotogenic model. This is achieved through a “hybrid mass mechanism” which is usually referred to as the “scoto-seesaw” mechanism¹ where the atmospheric scale arises from the tree-level seesaw, whereas the solar scale has a radiative scotogenic origin [28–36]. However, scoto-seesaw like other neutrino mass mechanisms, still requires the addition of a flavor symmetry to explain the leptonic mixing pattern [29, 31, 36]. In summary, usually, even the most simple and elegant BSM models require the addition of at least a new dark as well as a flavor symmetry, along with the associated expansion of the BSM particle content, to account for DM and to explain neutrino mass and flavor structure.

In this work, we develop a simple framework with a very minimal particle content, that can explain the DM stability, neutrino mass generation, and flavor structure of the lepton sector along with the two mass scales of neutrino oscillation experiments using only a single flavor symmetry. Within this framework, breaking of flavor symmetry induces a “scoto-seesaw” [28] like scenario, and DM stability is ensured by one of its unbroken subgroups. We demonstrate this idea by explicitly constructing a simple model with minimal particle content. We start by imposing the A_4 flavor symmetry on a scotogenic-like radiative loop as shown schematically in the left panel of Fig. 2. It is important to highlight that, unlike the \mathcal{Z}_2 symmetry of the scotogenic mechanism [10], which serves solely to stabilize DM candidate, the A_4 symmetry not only generates the flavor structure but also includes subgroups that fulfill the stabilizing role of \mathcal{Z}_2 . This makes A_4 a more comprehensive symmetry for achieving broader theoretical purposes. Such a flavor group can be connected to more fundamental groups like $SO(3)$ [37]. Additionally, it has been recently proposed that such a group could originate from finite modular groups Γ_N inspired by string theory and extra-dimensional models [38].

As shown in Fig. 2, both particles i.e. η and N running in the loop (left panel) transform as triplets under A_4 symmetry. The A_4 symmetry is then broken spontaneously by the vacuum expectation value (VEV) of the scalar η field in such a way as to leave a \mathcal{Z}_2 subgroup unbroken. The spontaneous breaking of A_4 symmetry to its residual \mathcal{Z}_2 subgroup amounts to cutting the radiative loop and leads to a hybrid scoto-seesaw mechanism as shown in the right panel of Fig. 2. The resulting scoto-seesaw mechanism implies that the neutrino masses are generated through contributions from both the tree-level type-I seesaw and the one-loop level scotogenic mechanism thus providing a natural explanation for the two different mass-squared differences observed in neutrino oscillation experiments. The unbroken \mathcal{Z}_2 symmetry plays the role of the scotogenic *dark* symmetry. The lightest \mathcal{Z}_2 odd particle is then automatically stable and can be a viable DM candidate.

In the leptonic sector, the A_4 flavor symmetry predicts a small range with a lower limit on the lightest neutrino mass, normal ordering of neutrino masses, and a “generalized μ – τ reflection symmetry” for the

¹ Note that the mass hierarchy among neutrinos is milder compared to that among different generations of other SM fermions. However, since $\frac{\Delta m_{\text{sol}}^2}{\Delta m_{\text{atm}}^2} \approx 10^{-2}$, this difference can have a natural explanation in terms of a hybrid mass generation mechanism such as “scoto-seesaw”.

neutrino mixing parameters that are in good agreement with recent data². We find testable predictions for the neutrino oscillations, neutrinoless double beta ($0\nu\beta\beta$) decay experiments along with beta decay experiments. Finally, the imprints of the emergence of the dark symmetry from the flavor symmetry can be found in the dark sector as well. For example, the particles within the dark sector in our model are constrained by an upper limit on their masses $\lesssim 600$ GeV. The fermionic DM case is completely ruled out by the constraints coming from the neutrino oscillation data. The scalar DM is also heavily constrained with the viable parameter space consistent with both neutrino and DM experimental results available only up to 80 GeV DM mass.

We structure the article as follows. In Sec. 2, we describe the general framework of our model. In Sec. 2.2.1 and 2.2.1, we present the potential and mass spectrum of the scalar sector, respectively. Sec. 2.2.3 discusses the generation of neutrino mass along with the neutrino flavor structure. In Sec. 3, we explain our numerical results for the neutrino sector. Our quantitative results for the dark sector are presented in Sec. 4. Finally, we give concluding remarks in Sec. 5. The A_4 algebra and expanded form of scalar potential are given in Appendix A, while detailed information regarding the fermionic DM case is provided in Appendix B. In Appendix C we discuss different choices of A_4 transformation of the leptonic doublets. The Feynman diagrams relevant to relic abundance and direct detection computations are in Appendix D.

2. MODEL SET-UP

We utilize a scotogenic-like radiative seesaw model in conjunction with A_4 flavor symmetry. In addition to being a popular flavor symmetry group, A_4 also has a \mathbb{Z}_2 subgroup which can potentially serve as the dark symmetry as we discuss later [41–44]. The field content and their transformations under the SM gauge group $SU(3)_C \otimes SU(2)_L \otimes U(1)_Y$ in addition to A_4 symmetry are provided in Table I. Notice that in Appendix C, we discuss various choices of A_4 transformations for the leptonic doublets. Contrary to the findings in [44], we highlight that the choice of A_4 transformations play a crucial role in predicting neutrino phenomenology.

Apart from SM particles, we introduce two types of BSM particles: $SU(2)_L$ doublet scalars η and singlet fermions N , both transforming as triplets under A_4 symmetry, see Appendix A 1 for more details of A_4 flavor symmetry. All SM particles transform as singlets under A_4 symmetry: the Higgs doublet Φ and all quarks transform as trivial singlet (1), and the charged leptons L_i and e_{R_i} ; $i = 1, 2, 3$ transform as singlets $(1, 1', 1'')$ under the A_4 symmetry. The charge assignment in Table I ensures that, after the A_4 symmetry breaking, all SM particles are even (+) under \mathbb{Z}_2 , given their singlet nature under

² It's important to note that the “ $\mu - \tau$ reflection symmetry”, initially introduced in [39], anticipates maximal values for both the Dirac CP phases and the atmospheric mixing angle. However, given that the best-fit values from neutrino oscillation data tend to favor non-maximal values for these parameters, the framework of “generalized $\mu - \tau$ reflection symmetry” [40] emerges as a successful model, showcasing its predictive capability.

Fields	$SU(3)_C \otimes SU(2)_L \otimes U(1)_Y$	$A_4 \rightarrow \mathcal{Z}_2$
L_i	(1, 2, -1)	$(1, 1', 1'') \rightarrow (+, +, +)$
e_{R_i}	(1, 1, -2)	$(1, 1', 1'') \rightarrow (+, +, +)$
Φ	(1, 2, 1)	$1 \rightarrow +$
η	(1, 2, 1)	$3 \rightarrow (+, -, -)$
N	(1, 1, 0)	$3 \rightarrow (+, -, -)$

TABLE I: Field content and their transformation properties under the SM gauge group $SU(3)_C \otimes SU(2)_L \otimes U(1)_Y$ and A_4 symmetry, where $i = 1, 2, 3$ represents generation indices. The A_4 group is spontaneously broken down to its \mathcal{Z}_2 subgroup by the VEV of the η scalar. Transformation properties of the residual \mathcal{Z}_2 symmetry are listed in the last column.

A_4 symmetry. The components of A_4 triplets η , N split into two, the first components transforming as even (+) while the other components have odd (-) charges under \mathcal{Z}_2 , see Appendix A1 for more details. Thus the particle content of our model is divided into even and odd particles under residual \mathcal{Z}_2 symmetry as shown in the last column of Table I. The odd particles will eventually become dark sector particles as discussed in Sec. 4.

2.1. Scalar sector

We start with the scalar sector of our model and discuss how the spontaneous breaking of A_4 symmetry leads to the emergence of residual \mathcal{Z}_2 dark symmetry. The $SU(3)_C \otimes SU(2)_L \otimes U(1)_Y \otimes A_4$ invariant scalar potential is given as follows:

$$\begin{aligned}
V = & \mu_\Phi^2 \Phi^\dagger \Phi + \mu_\eta^2 \left[\eta^\dagger \eta \right]_1 + \lambda_1 \left(\Phi^\dagger \Phi \right)^2 + \lambda_2 \left[\eta^\dagger \eta \right]_1^2 + \lambda_3 \left[\eta^\dagger \eta \right]_{1'} \left[\eta^\dagger \eta \right]_{1''} + \lambda_4 \left[\eta^\dagger \eta^\dagger \right]_{1'} [\eta \eta]_{1''} \\
& + \lambda_{4'} \left[\eta^\dagger \eta^\dagger \right]_{1''} [\eta \eta]_{1'} + \lambda_5 \left[\eta^\dagger \eta^\dagger \right]_1 [\eta \eta]_1 + \lambda_6 \left(\left[\eta^\dagger \eta \right]_{3_1} \left[\eta^\dagger \eta \right]_{3_1} + h.c. \right) + \lambda_7 \left[\eta^\dagger \eta \right]_{3_1} \left[\eta^\dagger \eta \right]_{3_2} \\
& + \lambda_8 \left[\eta^\dagger \eta^\dagger \right]_{3_1} [\eta \eta]_{3_2} + \lambda_9 \left[\eta^\dagger \eta \right]_1 \left(\Phi^\dagger \Phi \right) + \lambda_{10} \left[\eta^\dagger \Phi \right]_3 \left[\Phi^\dagger \eta \right]_3 + \lambda_{11} \left(\left[\eta^\dagger \eta^\dagger \right]_1 (\Phi \Phi) + h.c. \right) \\
& + \lambda_{12} \left(\left[\eta^\dagger \eta^\dagger \right]_{3_1} [\eta \Phi]_3 + h.c. \right) + \lambda_{13} \left(\left[\eta^\dagger \eta^\dagger \right]_{3_2} [\eta \Phi]_3 + h.c. \right) + \lambda_{14} \left(\left[\eta^\dagger \eta \right]_{3_1} \left[\eta^\dagger \Phi \right]_3 + h.c. \right) \\
& + \lambda_{15} \left(\left[\eta^\dagger \eta \right]_{3_2} \left[\eta^\dagger \Phi \right]_3 + h.c. \right) .
\end{aligned} \tag{1}$$

Where $[\dots]_p$; $p = 1, 1', 1'', 3, 3_1, 3_2$ denote the A_4 transformation of enclosed fields. Furthermore, $3_1, 3_2$ denote the two possible A_4 triplet contractions, see Eqs. (A3) and (A4) of Appendix A1.

Here it is important to emphasize a noteworthy aspect resulting from the A_4 symmetry. Specifically, terms of the form $\eta^3 \Phi$ are permitted by the A_4 symmetry. However in canonical scotogenic model [10] as well in its variants where the \mathcal{Z}_2 symmetry is explicitly added, they are forbidden due to the \mathcal{Z}_2 odd (even) charge assignment of η (Φ) fields. The presence of such terms in our model would eventually

lift the mass degeneracy between the components of the A_4 triplet η after the symmetry breaking. The expanded form of this potential in terms of the component fields is given in Appendix A 2.

Now coming to the breaking of A_4 symmetry, we aim to spontaneously break the A_4 symmetry in such a way that the \mathcal{Z}_2 subgroup remains unbroken. This can be accomplished by giving VEV to the A_4 triplet scalar η with the VEV alignment $\langle \eta \rangle = \frac{1}{\sqrt{2}}(v_2, 0, 0)$. Furthermore, after $A_4 \rightarrow \mathcal{Z}_2$ breaking, the components η_i ; $i = 1, 2, 3$ split into two types under the residual \mathcal{Z}_2 symmetry, transforming as

$$\eta_1 \rightarrow +\eta_1, \quad \eta_2 \rightarrow -\eta_2, \quad \eta_3 \rightarrow -\eta_3 \quad (2)$$

while Φ being a A_4 singlet transform as $\Phi \rightarrow +\Phi$ under the residual \mathcal{Z}_2 . The transformations of various representations of A_4 under the \mathcal{Z}_2 subgroup are given in Appendix A 1.

Since η is a $SU(2)_L$ doublet, its VEV also breaks the electroweak symmetry along with the VEV of Φ . Thus, the scalars have the following VEV alignments:

$$\langle \Phi \rangle = \frac{v_1}{\sqrt{2}}, \quad \langle \eta_1 \rangle = \frac{v_2}{\sqrt{2}} \text{ and } \langle \eta_2 \rangle = \langle \eta_3 \rangle = 0. \quad (3)$$

We define $\tan \beta = v_2/v_1$ and we will take $\tan \beta \sim 1$ in the rest of the analysis. The potential is also CP conserving if all couplings are taken to be real and $\lambda_{4'} = \lambda_4$. The requirement of perturbativity leads to the constraints on the λ_i couplings and $\tan \beta$ given by:

$$\lambda_i \lesssim \sqrt{4\pi}, \quad i = 1, \dots, 15, \quad \tan \beta > 0.5. \quad (4)$$

The tree-level stability of the vacuum can be ensured by the following conditions [42]:

$$\begin{aligned} \lambda_1 &> 0, \quad \lambda_2 + \lambda_3 + 2\lambda_4 + \lambda_5 > 0, \\ \lambda_1 + 3(\lambda_2 + \lambda_3 + 2\lambda_4 + \lambda_5) + 3(\lambda_9 + Q_1) + 3(2\lambda_2 - \lambda_3 + \lambda_8 + Q_2) - 6\zeta &> 0, \end{aligned} \quad (5)$$

where $Q_1 = \text{Min}(\lambda_{10} - 2|\lambda_{11}|, 0)$, $Q_2 = \text{Min}(\lambda_7 - 2|\lambda_4 - \lambda_5 - \lambda_6|, 0)$ and $\zeta = |\lambda_{12}| + |\lambda_{13}| + |\lambda_{14}| + |\lambda_{15}|$. The last line of Eq. (5) is an approximate condition for the stability which can be obtained following the procedure discussed in [45–47].

The $SU(2)_L$ doublet scalars Φ and η_i after SSB, are expressed as:

$$\begin{aligned} \Phi &= \begin{pmatrix} \phi^+ \\ (v_1 + \phi^0 + i\sigma_1^0)/\sqrt{2} \end{pmatrix}, \quad \eta_1 = \begin{pmatrix} \eta_1^+ \\ (v_2 + \eta_1^R + i\eta_1^I)/\sqrt{2} \end{pmatrix}, \\ \eta_2 &= \begin{pmatrix} \eta_2^+ \\ (\eta_2^R + i\eta_2^I)/\sqrt{2} \end{pmatrix}, \quad \eta_3 = \begin{pmatrix} \eta_3^+ \\ (\eta_3^R + i\eta_3^I)/\sqrt{2} \end{pmatrix}. \end{aligned} \quad (6)$$

Note that η_2 and η_3 transform as $(-)$ under the residual \mathcal{Z}_2 subgroup and have not acquired any VEV, ensuring \mathcal{Z}_2 survives as a residual symmetry after the A_4 symmetry breaking.

2.2. Mass spectrum of scalars

After SSB the scalars acquire masses which can be computed using the scalar potential (1) together with the Eqs. (3) and (6). To simplify our expressions for masses of the scalars, we define the following combinations of couplings:

$$\begin{aligned}
\Lambda &= \lambda_2 + \lambda_3 + 2\lambda_4 + \lambda_5, \\
\kappa_1 &= (-3\lambda_3 - 6\lambda_4 + 2\lambda_6 + \lambda_7 + \lambda_8), \\
\kappa_2 &= (-3\lambda_3 - 2\lambda_4 - 4\lambda_5 - 2\lambda_6 + \lambda_7 + \lambda_8), \\
\kappa_3 &= (-3\lambda_3 - 4\lambda_4 - 2\lambda_5 + \lambda_8), \\
\alpha &= \lambda_9 + \lambda_{10} + 2\lambda_{11}, \\
\zeta &= \lambda_{12} + \lambda_{13} + \lambda_{14} + \lambda_{15}.
\end{aligned} \tag{7}$$

The mass matrix for the CP even electrically neutral scalars in the basis $(\phi^0, \eta_1^R, \eta_2^R, \eta_3^R)$ and $(\phi^0, \eta_1^R, \eta_2^R, \eta_3^R)^T$ has a block diagonal form given as follows:

$$\mathcal{M}_{neutral}^R = \begin{pmatrix} \mathcal{M}_{H_1 H_2} & 0 \\ 0 & \mathcal{M}_{\eta_2^R \eta_3^R} \end{pmatrix}. \tag{8}$$

Note that the block diagonal form of $\mathcal{M}_{neutral}^R$ is a reflection of the unbroken residual \mathcal{Z}_2 symmetry. Recall that Φ and η_1 are \mathcal{Z}_2 even while η_2 and η_3 are \mathcal{Z}_2 odd. Since the \mathcal{Z}_2 symmetry remains unbroken, the even particles are mixing with each other, and odd particles mix among themselves leading to this peculiar block diagonal form. The matrices $\mathcal{M}_{H_1 H_2}$ and $\mathcal{M}_{\eta_2^R \eta_3^R}$ are given by:

$$\mathcal{M}_{H_1 H_2} = \begin{pmatrix} 2\lambda_1 v_1^2 & \alpha v_1 v_2 \\ \alpha v_1 v_2 & 2\Lambda v_2^2 \end{pmatrix}, \quad \mathcal{M}_{\eta_2^R \eta_3^R} = \frac{1}{2} \begin{pmatrix} \kappa_1 v_2^2 & 3\zeta v_1 v_2 \\ 3\zeta v_1 v_2 & \kappa_1 v_2^2 \end{pmatrix}. \tag{9}$$

The mass matrix for CP odd electrically neutral scalars in the basis $(\sigma_1^0, \eta_1^I, \eta_2^I, \eta_3^I)$ and $(\sigma_1^0, \eta_1^I, \eta_2^I, \eta_3^I)^T$ as well as the charged scalars mass matrix in the basis $(\phi^-, \eta_1^-, \eta_2^-, \eta_3^-)$ and $(\phi^+, \eta_1^+, \eta_2^+, \eta_3^+)^T$ are expressed as:

$$\mathcal{M}_{neutral}^I = \begin{pmatrix} \mathcal{M}_{GA} & 0 \\ 0 & \mathcal{M}_{\eta_2^I \eta_3^I} \end{pmatrix}, \quad \mathcal{M}_{charged} = \begin{pmatrix} \mathcal{M}_{G^\pm H^\pm} & 0 \\ 0 & \mathcal{M}_{\eta_2^\pm \eta_3^\pm} \end{pmatrix}. \tag{10}$$

Again the block diagonal form of these matrices reflects their transformation under the unbroken \mathcal{Z}_2

symmetry. The four matrices \mathcal{M}_{GA} , $\mathcal{M}_{\eta_2^I \eta_3^I}$, $\mathcal{M}_{G^\pm H^\pm}$ and $\mathcal{M}_{\eta_2^\pm \eta_3^\pm}$ are given as:

$$\begin{aligned}\mathcal{M}_{GA} &= -2\lambda_{11} \begin{pmatrix} v_2^2 & -v_1 v_2 \\ -v_1 v_2 & v_1^2 \end{pmatrix}, \quad \mathcal{M}_{\eta_2^I \eta_3^I} = \frac{1}{2} \begin{pmatrix} \kappa_2 v_2^2 - 4\lambda_{11} v_1^2 & \zeta v_1 v_2 \\ \zeta v_1 v_2 & \kappa_2 v_2^2 - 4\lambda_{11} v_1^2 \end{pmatrix}, \\ \mathcal{M}_{G^\pm H^\pm} &= -\frac{(\lambda_{10} + 2\lambda_{11})}{2} \begin{pmatrix} v_2^2 & -v_1 v_2 \\ -v_1 v_2 & v_1^2 \end{pmatrix}, \\ \mathcal{M}_{\eta_2^\pm \eta_3^\pm} &= \frac{1}{2} \begin{pmatrix} \kappa_3 v_2^2 - (\lambda_{10} + 2\lambda_{11}) v_1^2 & \zeta v_1 v_2 \\ \zeta v_1 v_2 & \kappa_3 v_2^2 - (\lambda_{10} + 2\lambda_{11}) v_1^2 \end{pmatrix}.\end{aligned}\tag{11}$$

The matrices \mathcal{M}_{GA} and $\mathcal{M}_{G^\pm H^\pm}$ both have one vanishing eigenvalue (i.e., these are rank-1 matrices) corresponding to the neutral and charged Goldstone bosons corresponding to the Z and W^\pm gauge bosons, respectively. After diagonalization, the mass spectrum of the physical particles becomes:

$$\begin{aligned}m_{H_1, H_2}^2 &= \lambda_1 v_1^2 + \Lambda v_2^2 \mp \sqrt{(\lambda_1 v_1^2 + \Lambda v_2^2)^2 + v_1^2 v_2^2 (\alpha^2 - 4\Lambda \lambda_1)}, \\ m_A^2 &= -2\lambda_{11} (v_1^2 + v_2^2), \quad m_G^2 = 0, \\ m_{H^\pm}^2 &= -(\lambda_{10} + 2\lambda_{11}) (v_1^2 + v_2^2) / 2, \quad m_{G^\pm}^2 = 0, \\ m_{\eta_2^R}^2 &= (\kappa_1 v_2^2 - 3\zeta v_1 v_2) / 2, \quad m_{\eta_2^I}^2 = (\kappa_2 v_2^2 - 4\lambda_{11} v_1^2 - \zeta v_1 v_2) / 2, \\ m_{\eta_3^R}^2 &= m_{\eta_2^R}^2 + 3\zeta v_1 v_2, \quad m_{\eta_3^I}^2 = m_{\eta_2^I}^2 + \zeta v_1 v_2, \\ m_{\eta_2^\pm}^2 &= (\kappa_3 v_2^2 - (\lambda_{10} + 2\lambda_{11}) v_1^2 - \zeta v_1 v_2) / 2, \quad m_{\eta_3^\pm}^2 = m_{\eta_2^\pm}^2 + \zeta v_1 v_2.\end{aligned}\tag{12}$$

We identify H_1 as the SM like Higgs and take its mass 125.25 ± 0.17 GeV [48] throughout the whole discussion. From Eqs. (12) and (7), it becomes evident that the masses of the scalars are exclusively determined by the VEVs and the quartic λ couplings. Since the λ s are constrained by the perturbativity condition Eq. (4), it imposes a theoretical upper limit $m_{\text{scalar}} \approx \lambda_i v \approx \sqrt{4\pi} \times 246 / \sqrt{2} \text{ GeV} \lesssim 600 \text{ GeV}$ on all scalar masses³ [42]. This implies that the DM mass in our model has an upper bound $\lesssim 600 \text{ GeV}$ ⁴. This distinctive feature of our model is a direct consequence of the A_4 flavor symmetric approach, which distinguishes it from other scotogenic as well as (inert) Two-Higgs-Doublet models.

2.3. Neutrino sector

Having discussed the spontaneous $A_4 \rightarrow \mathcal{Z}_2$ breaking and the scalar mass spectrum, we now turn to the generation of neutrino masses. According to the charge assignment outlined in Table I, the $SU(3)_C \otimes SU(2)_L \otimes U(1)_Y \otimes A_4$ invariant Yukawa Lagrangian that describes the leptonic sector can

³ This limit exists in our model because we have broken the A_4 symmetry only spontaneously. The addition of soft A_4 symmetry breaking terms in the potential can allow us to have scalar and DM masses larger than this limit [49].

⁴ Even if DM is fermionic, this upper limit on its mass still applies as the DM has to be the lightest particle in the dark sector. Since all \mathcal{Z}_2 odd scalars have their masses $\lesssim 600 \text{ GeV}$, the fermionic DM should also be $\lesssim 600 \text{ GeV}$.

be expressed as follows:

$$\begin{aligned}
-\mathcal{L}_y = & y_{11}(\bar{L}_1)_1 \Phi(e_{R_1})_1 + y_{22}(\bar{L}_2)_{1''} \Phi(e_{R_2})_{1'} + y_{33}(\bar{L}_3)_{1'} \Phi(e_{R_3})_{1''} + y_1(\bar{L}_1)_1 (\tilde{\eta}N)_1 \\
& + y_2(\bar{L}_2)_{1''} (\tilde{\eta}N)_{1'} + y_3(\bar{L}_3)_{1'} (\tilde{\eta}N)_{1''} + M(\bar{N}^c N)_1 + h.c. ,
\end{aligned} \tag{13}$$

where subscript $(\cdots)_{1/1'/1''}$ denotes the A_4 transformation properties of the fields enclosed inside the parentheses. In terms of their components, the above Lagrangian can be written as follows:

$$\begin{aligned}
-\mathcal{L}_y = & y_{11}(\bar{L}_1)_1 \Phi(e_{R_1})_1 + y_{22}(\bar{L}_2)_{1''} \Phi(e_{R_2})_{1'} + y_{33}(\bar{L}_3)_{1'} \Phi(e_{R_3})_{1''} \\
& + y_1(\bar{L}_1)_1 \left(\begin{pmatrix} \tilde{\eta}_1 \\ \tilde{\eta}_2 \\ \tilde{\eta}_3 \end{pmatrix}_3 \begin{pmatrix} N_1 \\ N_2 \\ N_3 \end{pmatrix}_3 \right)_1 + y_2(\bar{L}_2)_{1''} \left(\begin{pmatrix} \tilde{\eta}_1 \\ \tilde{\eta}_2 \\ \tilde{\eta}_3 \end{pmatrix}_3 \begin{pmatrix} N_1 \\ N_2 \\ N_3 \end{pmatrix}_3 \right)_{1'} \\
& + y_3(\bar{L}_3)_{1'} \left(\begin{pmatrix} \tilde{\eta}_1 \\ \tilde{\eta}_2 \\ \tilde{\eta}_3 \end{pmatrix}_3 \begin{pmatrix} N_1 \\ N_2 \\ N_3 \end{pmatrix}_3 \right)_{1''} + M \left(\begin{pmatrix} \bar{N}_1^c \\ \bar{N}_2^c \\ \bar{N}_3^c \end{pmatrix}_3 \begin{pmatrix} N_1 \\ N_2 \\ N_3 \end{pmatrix}_3 \right)_1 + h.c. ,
\end{aligned} \tag{14}$$

which using A_4 multiplication rules of Appendix A 1 can be further expanded as:

$$\begin{aligned}
-\mathcal{L}_y = & y_{11}\bar{L}_1\Phi e_{R_1} + y_{22}\bar{L}_2\Phi e_{R_2} + y_{33}\bar{L}_3\Phi e_{R_3} + y_1\bar{L}_1(\tilde{\eta}_1 N_1 + \tilde{\eta}_2 N_2 + \tilde{\eta}_3 N_3) \\
& + y_2\bar{L}_2(\tilde{\eta}_1 N_1 + \omega\tilde{\eta}_2 N_2 + \omega^2\tilde{\eta}_3 N_3) + y_3\bar{L}_3(\tilde{\eta}_1 N_1 + \omega^2\tilde{\eta}_2 N_2 + \omega\tilde{\eta}_3 N_3) \\
& + M(\bar{N}_1^c N_1 + \bar{N}_2^c N_2 + \bar{N}_3^c N_3) + h.c. .
\end{aligned} \tag{15}$$

where $\tilde{\eta} = i\tau_2\eta^*$; τ_2 is the second Pauli matrix and y_{ii} , y_i for $i = 1, 2, 3$ are the Yukawa couplings, ω is the cubic root of unity and M is the Majorana mass of fermion N .

As discussed in Sec. 2.2.1 the A_4 symmetry is broken to the residual \mathcal{Z}_2 subgroup by the VEV of the first component, η_1 of the triplet η , while the other two components η_2 and η_3 do not acquire VEV. Since, N is also a triplet of A_4 , after the A_4 symmetry is broken, its components transform as

$$N_1 \rightarrow +N_1, \quad N_2 \rightarrow -N_2, \quad N_3 \rightarrow -N_3. \tag{16}$$

under the residual \mathcal{Z}_2 subgroup. The lepton doublets (L_i) and charged lepton singlets (e_{R_i}) ; $i = 1, 2, 3$ being A_4 singlets, will be even under the residual \mathcal{Z}_2 subgroup. Hence the charged leptons get masses through the standard Higgs mechanism and they can also mix among themselves. However, due to the specific charge assignment of charged leptons under A_4 , the charged lepton mass matrix is diagonal and is written as $M_l = v_1 \text{diag}(y_{11}, y_{22}, y_{33})/\sqrt{2}$. Therefore, the observed oscillation and mixing pattern of leptons arises from the neutrino sector only.

Coming to the neutrino mass generation, when the A_4 symmetry is unbroken, one can have a radiative loop as shown in the left panel of Fig. 2. However, since $\langle \eta_1 \rangle = \frac{v_2}{\sqrt{2}} \neq 0$, the spontaneous breaking of $A_4 \rightarrow \mathcal{Z}_2$ leads to “cutting” of this radiative loop. This breaking pattern leads to the hybrid

scoto-seesaw mass generation where neutrinos get mass both from a type-I seesaw as well as from the scotogenic loop as shown in the right panel of Fig. 2. This happens because after SSB the η_1 field being \mathcal{Z}_2 even mixes with Φ and results in the type-I like seesaw diagram where the \mathcal{Z}_2 even fermion N_1 acts as an intermediate connection as shown in the upper part of the right panel of Fig. 2. The \mathcal{Z}_2 odd fermions $N_{2,3}$ and scalars $\eta_{2,3}$ now belong to the dark sector and they together run inside a radiative loop as depicted in the lower right panel of Fig. 2. The conserved \mathcal{Z}_2 symmetry then ensures that the lightest particle running inside the loop can be a good DM candidate.

At the tree-level the mass matrix in the basis of $(\bar{\nu}_1^c, \bar{\nu}_2^c, \bar{\nu}_3^c, \bar{N}_1^c, \bar{N}_2^c, \bar{N}_3^c)$ and

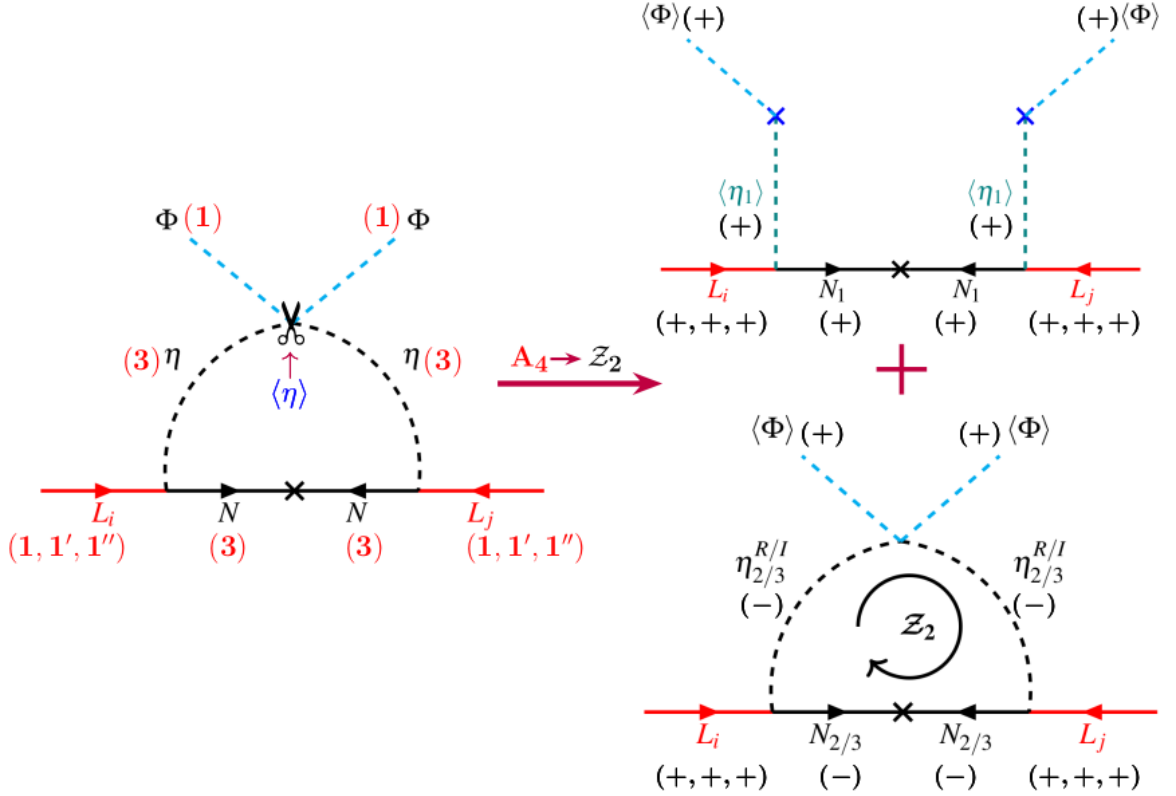


FIG. 2: Schematic diagram showing how $A_4 \rightarrow \mathcal{Z}_2$ cuts the scotogenic loop leading to a hybrid scoto-seesaw mass mechanism. The left panel is flavor A_4 invariant with both particles (η, N) running inside the loop being triplets of the A_4 group. The right panel is invariant under the residual \mathcal{Z}_2 subgroup which also serves as the dark symmetry. The A_4 symmetry is broken spontaneously to a residual \mathcal{Z}_2 subgroup by the VEV of the scalar η , thus cutting the radiative loop. This results in a scoto-seesaw mass mechanism i.e., a type-I seesaw and a one-loop level radiative model as shown in the right panel. The residual \mathcal{Z}_2 subgroup running inside the loop serves as the dark symmetry. Before (after) symmetry breaking A_4 (\mathcal{Z}_2) charges have been shown in the left (right) panel of the diagram.

$(\nu_1, \nu_2, \nu_3, N_1, N_2, N_3)^T$ is given by

$$\mathcal{M}_\nu = \frac{1}{\sqrt{2}} \begin{pmatrix} 0 & 0 & 0 & y_1 v_2 & 0 & 0 \\ 0 & 0 & 0 & y_2 v_2 & 0 & 0 \\ 0 & 0 & 0 & y_3 v_2 & 0 & 0 \\ y_1 v_2 & y_2 v_2 & y_3 v_2 & \sqrt{2}M & 0 & 0 \\ 0 & 0 & 0 & 0 & \sqrt{2}M & 0 \\ 0 & 0 & 0 & 0 & 0 & \sqrt{2}M \end{pmatrix}. \quad (17)$$

Note that the zeros in off-diagonal terms in \mathcal{M}_ν are due to the conserved \mathcal{Z}_2 symmetry which forbids coupling between even (ν_i, N_1) and odd (N_2, N_3) fields. The mass matrix in Eq. (17) can be further blocked diagonalized in the type-I seesaw limit. The resulting light neutrino mass matrix can be expressed as

$$-m_\nu^{(1)} = m_D \mathcal{M}^{-1} m_D^T = \frac{v_2^2}{2M} \begin{pmatrix} y_1^2 & y_1 y_2 & y_1 y_3 \\ * & y_2^2 & y_2 y_3 \\ * & * & y_3^2 \end{pmatrix}. \quad (18)$$

$$\text{where, } m_D = \frac{v_2}{\sqrt{2}} \begin{pmatrix} y_1 & 0 & 0 \\ y_2 & 0 & 0 \\ y_3 & 0 & 0 \end{pmatrix}, \quad \mathcal{M} = \text{diag } M(1, 1, 1). \quad (19)$$

Note that just like in canonical type-I seesaw, the mass of fermion N_1 also gets a small seesaw correction and will change slightly from the M value, whereas the tree-level masses of the other two fermions N_2 and N_3 will remain M because of A_4 symmetry. Eventually, the degeneracy in N_2, N_3 masses is also slightly lifted due to the loop corrections.

Coming back to the light neutrino mass matrix $m_\nu^{(1)}$, one can immediately notice that the rank of $m_\nu^{(1)}$ is one and hence only one of the neutrinos gets mass through this type-I seesaw diagram. However, the masses of neutrinos also get contribution from the one-loop diagram as shown by Fig. 2. The additional mass matrix arising from the one-loop is given by [10]

$$(\mathcal{M}_\nu)_{ij} = \sum_{l,k=1}^3 \frac{Y_{ik} Y_{jk}}{32\pi^2} M_k \left[\frac{(m_{\eta_l}^R)^2}{(m_{\eta_l}^R)^2 - M_k^2} \ln \left(\frac{m_{\eta_l}^R}{M_k} \right)^2 - \frac{(m_{\eta_l}^I)^2}{(m_{\eta_l}^I)^2 - M_k^2} \ln \left(\frac{m_{\eta_l}^I}{M_k} \right)^2 \right]. \quad (20)$$

Because of A_4 symmetry in our model, we have $l = k$. Thus the mass matrix is simplified to

$$(\mathcal{M}_\nu)_{ij} = \sum_{k=1}^3 Y_{ik} Y_{jk} c_k, \quad (21)$$

where, Y_{ik} and Y_{jk} are Yukawa couplings at one-loop level, and

$$c_k = \frac{M_k}{32\pi^2} \left[\frac{(m_{\eta_k}^R)^2}{(m_{\eta_k}^R)^2 - M_k^2} \ln \left(\frac{m_{\eta_k}^R}{M_k} \right)^2 - \frac{(m_{\eta_k}^I)^2}{(m_{\eta_k}^I)^2 - M_k^2} \ln \left(\frac{m_{\eta_k}^I}{M_k} \right)^2 \right]. \quad (22)$$

The couplings Y_{ik} and Y_{jk} are given by

$$\begin{aligned} Y_{11} &= y_1, & Y_{12} &= y_1, & Y_{13} &= y_1, \\ Y_{21} &= y_2, & Y_{22} &= \omega y_2, & Y_{23} &= \omega^2 y_2, \\ Y_{31} &= y_3, & Y_{32} &= \omega^2 y_3, & Y_{33} &= \omega y_3. \end{aligned} \quad (23)$$

Substituting (23) in (21) and simplifying, we get

$$\begin{aligned} (\mathcal{M}_\nu)_{11} &= y_1^2 (c_1 + c_2 + c_3), & (\mathcal{M}_\nu)_{12} &= y_1 y_2 (c_1 + \omega c_2 + \omega^2 c_3), & (\mathcal{M}_\nu)_{13} &= y_1 y_3 (c_1 + \omega^2 c_2 + \omega c_3), \\ (\mathcal{M}_\nu)_{21} &= y_2 y_1 (c_1 + \omega c_2 + \omega^2 c_3), & (\mathcal{M}_\nu)_{22} &= y_2^2 (c_1 + \omega^2 c_2 + \omega c_3), & (\mathcal{M}_\nu)_{23} &= y_2 y_3 (c_1 + c_2 + c_3), \\ (\mathcal{M}_\nu)_{31} &= y_3 y_1 (c_1 + \omega^2 c_2 + \omega c_3), & (\mathcal{M}_\nu)_{32} &= y_3 y_2 (c_1 + c_2 + c_3), & (\mathcal{M}_\nu)_{33} &= y_3^2 (c_1 + \omega c_2 + \omega^2 c_3). \end{aligned} \quad (24)$$

Thus, the light neutrino mass matrix arising from the one-loop level is given by:

$$m_\nu^{(2)} = \begin{pmatrix} y_1^2 d_1 & y_1 y_2 d_2 & y_1 y_3 d_3 \\ * & y_2^2 d_3 & y_2 y_3 d_1 \\ * & * & y_3^2 d_2 \end{pmatrix}. \quad (25)$$

$$\text{where,} \quad d_1 = c_1 + c_2 + c_3, \quad d_2 = c_1 + \omega c_2 + \omega^2 c_3, \quad d_3 = c_1 + \omega^2 c_2 + \omega c_3. \quad (26)$$

Note that here d_1 is real, whereas due to the presence of ω and ω^2 , d_2 and d_3 are complex conjugates of each other. The expressions of c_1 , c_2 , c_3 can be derived from Eq. (22). It is to be noted here that as all the Yukawa couplings are considered real, the CP violation in the leptonic sector arises from the complex nature of d_2 and d_3 only.

Combining both the tree-level seesaw as well as one-loop level scotogenic contributions, the ‘‘scoto-seesaw’’ mass matrix for the light neutrinos can be expressed as:

$$m_\nu^{(TOT)} = m_\nu^{(1)} + m_\nu^{(2)} \equiv \begin{pmatrix} A & C & \tilde{C} \\ * & B & D \\ * & * & \tilde{B} \end{pmatrix}. \quad (27)$$

where,

$$\begin{aligned}
A &= y_1^2 \left(d_1 - \frac{v_2^2}{2M} \right), & D &= y_2 y_3 \left(d_1 - \frac{v_2^2}{2M} \right), \\
B &= y_2^2 \left(d_3 - \frac{v_2^2}{2M} \right), & \tilde{B} &= y_3^2 \left(d_2 - \frac{v_2^2}{2M} \right), \\
C &= y_1 y_2 \left(d_2 - \frac{v_2^2}{2M} \right), & \tilde{C} &= y_1 y_3 \left(d_3 - \frac{v_2^2}{2M} \right).
\end{aligned} \tag{28}$$

By virtue of d_1 being real and d_2, d_3 being conjugates of each other, the parameters A and D are real, whereas parameters B, \tilde{B}, C and \tilde{C} are complex.

3. NUMERICAL RESULTS FOR NEUTRINO SECTOR

In this section we aim to discuss our main results and predictions for the neutrino sector. To begin with, note that, in the scoto-seesaw models the Yukawa couplings appearing in the seesaw part and those appearing in the scotogenic part are independent of each other [28, 30]. Thus, in general, the typical scoto-seesaw models allow for two types of limiting cases depending upon the fermion masses:

- **Case-I:** Scalar masses m_{η_i} in GeV-TeV range, fermion masses, $M_i \sim m_{\eta_i}$.
- **Case-II:** Scalar masses m_{η_i} in GeV-TeV range, fermion masses, $M_i \gg m_{\eta_i}$.

From the purely aesthetic point of view, the case-I is less appealing as it necessarily requires smaller Yukawa couplings in the $\sim 10^{-8} - 10^{-6}$ range while case-II allows for Yukawa couplings up to $\mathcal{O}(1)$. However, both limits are perfectly allowed by the canonical scoto-seesaw model and its variants.

In our case, due to the A_4 symmetry, the same Yukawa couplings (see (15) and discussion in Sec. 2.2.3) appear in both seesaw and scotogenic parts. Thus our model is more constrained than typical scoto-seesaw models. In fact, during the numerical analysis, we found that if the masses of the fermions (N_1, N_2, N_3) are $\leq 10^5$ GeV, we can not simultaneously satisfy the two mass-squared differences Δm_{atm}^2 and Δm_{sol}^2 of neutrino oscillations within their current 3σ range, see Appendix B for more details. Therefore, in our model, case-I is automatically ruled out as only higher values of fermion masses $m_{N_i} \gg m_{\eta_i}$ can fit the observed neutrino oscillation constraints. This also implies that the fermionic dark matter case where $m_{N_i} < m_{\eta_i} \lesssim 600$ GeV is also ruled out as discussed in Appendix B.

To perform the numerical analysis the input parameters are varied following Table II. The value of Higgs mass has been fixed within its experimental 3σ range 125.25 ± 0.17 GeV [48], whereas all other scalars masses have been varied up to 600 GeV, keeping η_2^R as the lightest dark sector particle, hence a good DM candidate. While the neutrino sector constraints primarily depend on the masses of N_i and the Yukawa couplings, the λ s will play a key role in the dark sector analysis, see Sec. 4.

Parameters	Range	Parameters	Range
$M_{1,2,3}$ (in GeV)	$[10^6, 10^{12}]$	y_i	$[10^{-6}, 10^{-2}]$
λ_1	$[10^{-3}, \sqrt{4\pi}]$	$ \lambda_{2,3,\dots,10} $	$[10^{-6}, \sqrt{4\pi}]$
λ_{11}	$-[10^{-6}, \sqrt{4\pi}]$	$\lambda_{12,13,14,15}$	$[10^{-8}, 10^{-2}]$

TABLE II: Value range for the numerical parameter scan in the neutrino sector.

After performing the numerical analysis we find that our results are in good agreement with the three mixing angles (θ_{12} , θ_{13} , and θ_{23}) as well as two mass-squared differences (Δm_{atm}^2 and Δm_{sol}^2) of neutrino oscillation data [6–8] only for normal ordering (NO) of neutrino masses. Therefore all our results are obtained using NO of neutrino masses.

3.1. Predictions for CP phases

In this section we discuss how A_4 symmetry leads to predictions regarding the flavor structure of neutrinos. We start with observing that the mass matrix in Eq. (27), for $\tilde{B} = B^*$ and $\tilde{C} = C^*$, becomes $\mu - \tau$ reflection symmetric [39]. In this limit the atmospheric mixing angle, $\theta_{23} = 45^\circ$ and Dirac CP phase $\delta_{\text{CP}} = \pi/2$ or $3\pi/2$. From Eq. (28) we see that since d_2 and d_3 are complex conjugate to each other, thus the condition for the $\mu - \tau$ reflection symmetry i.e. $\tilde{B} = B^*$ and $\tilde{C} = C^*$ is obtained simply when the Yuakwa couplings $y_2 = y_3$. The exact $\mu - \tau$ reflection symmetry limit is shown by the intersection of dotted-black lines in the left panel of Fig. 3.

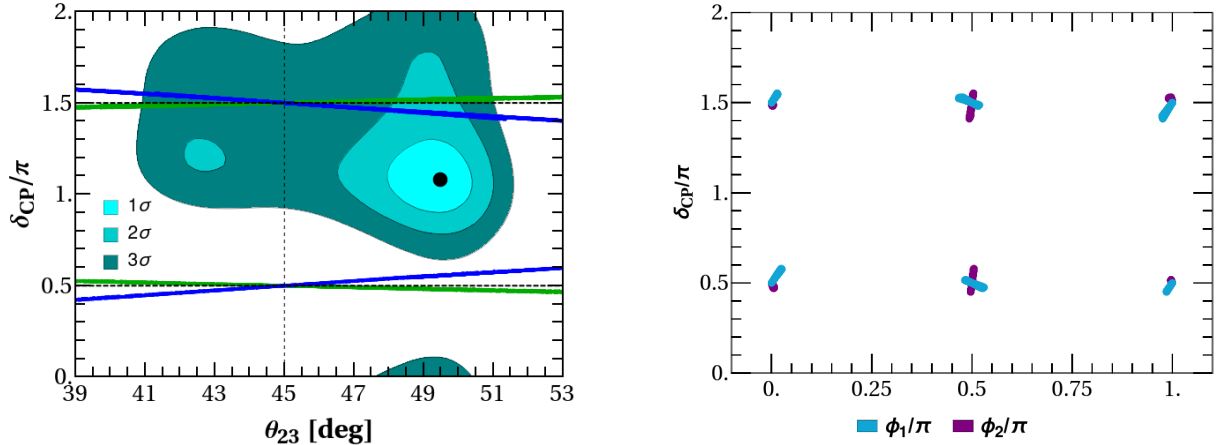


FIG. 3: **Left panel:** Predictions of the model in the $(\theta_{23} - \delta_{\text{CP}})$ plane are shown by the green and blue points. The cyan-colored contours correspond to the current 1, 2, 3 σ confidence level of the latest global-fit data [7]. The intersection of dotted-black lines corresponds to the exact $\mu - \tau$ reflection symmetry limit. **Right panel:** Correlation between Dirac (δ_{CP}) vs Majorana CP phases (ϕ_1, ϕ_2) are shown.

In general, the two Yukawa couplings y_2 and y_3 are independent parameters and can have different

values. Whenever $y_2 \neq y_3$ in the neutrino mass matrix (see Eq. (27)), we depart from the exact $\mu - \tau$ reflection symmetry. Thus our model leads to the “generalized $\mu - \tau$ reflection symmetry” as shown by the green and blue points in the left panel of Fig. 3. Depending upon the choice of y_2 and y_3 , the mixing angle θ_{23} will shift to lower or upper octant as follows:

$$\begin{aligned} y_2 < y_3 &\Rightarrow \theta_{23} < 45^\circ, \\ y_2 > y_3 &\Rightarrow \theta_{23} > 45^\circ. \end{aligned} \tag{29}$$

Note that in Fig. 3 both green and blue points lie very close to maximal δ_{CP} values predicting large CP violation in the leptonic sector. Furthermore, they are symmetric with respect to reflection around $\delta_{\text{CP}} = \pi$ value. The gaps between the two sets of points correspond to points that fail to either satisfy the 3σ constraints of the other two mixing angles θ_{12} and θ_{13} or the two mass-squared differences, leading to the splitting between the green and blue points. For comparison, we also show the latest global analysis of neutrino oscillation data [7] using the cyan color contours. It can be inferred that only the solutions around $\delta_{\text{CP}} = 1.5\pi$ are consistent with the latest neutrino data at 3σ significance level. This can serve as an important test of our model as an improved measurement of δ_{CP} significantly away from 1.5π value cannot be explained by our model. Indeed future experiments like DUNE [50] can measure δ_{CP} with much higher accuracy and can confirm or rule out our model entirely.

In the right panel, we have shown the correlation of the Dirac CP phase δ_{CP} with the Majorana CP phases ϕ_1 and ϕ_2 . From here, it is evident that both the Majorana CP phases are highly constrained and lie close to their CP-conserving values. This pattern can also be understood by recalling that in the exact $\mu - \tau$ reflection symmetry limit, the Majorana phases can have only 0 or $\frac{\pi}{2}$ values. Since our model has generalized $\mu - \tau$ reflection symmetry, the phases deviate by a small amount from their exact $\mu - \tau$ reflection symmetry limit. The importance of these highly constrained Majorana phases will be analyzed for $0\nu\beta\beta$ decay.

3.2. Lower limit on the lightest neutrino mass

In our model, we also have the prediction for the lightest neutrino mass $m_{\text{lightest}} = m_1$, shown in Fig. 4.

To illustrate that, we present a correlation plot between m_1 and mixing angle θ_{12} using the green and blue points. The reason behind these two sets remains the same as the left panel of Fig. 3. From Fig. 4, one can see that once we impose the 3σ range of θ_{12} from the global fit data (see the pink region), we find a small range for the m_1 mass. We find the lowest allowed values as $m_1 \sim 1.5$ (3.35) meV from the blue (green) points. It is important to note that these minimum allowed values of neutrino mass are crucial for predicting the effective Majorana neutrino mass in $0\nu\beta\beta$ decay, a topic that will be discussed in the following section.

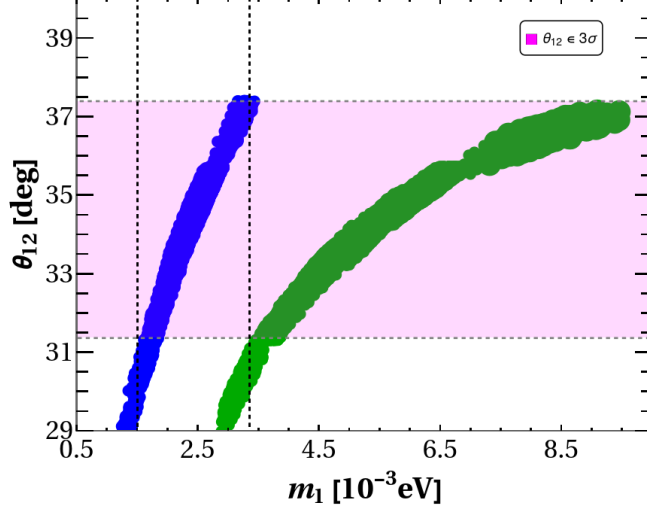


FIG. 4: Correlation between mixing angle θ_{12} and the lightest neutrino mass $m_{\text{lightest}} = m_1$.

3.3. Predictions for $0\nu\beta\beta$ decay and beta decay

Turning to other observables in the neutrino sector, one of the most important to consider is neutrinoless double beta decay ($0\nu\beta\beta$) which is a robust way for searching for lepton number violation and Majorana nature of neutrinos [51]. The half-life of $0\nu\beta\beta$ process is given by

$$\frac{1}{T_{1/2}^{0\nu}} = G_{0\nu} |M_{0\nu}(A, Z)|^2 |\langle m_{ee} \rangle|^2. \quad (30)$$

where, $G_{0\nu}$ represents the two-body phase-space factor, $M_{0\nu}$ is the nuclear matrix element and $\langle m_{ee} \rangle$ is the effective Majorana neutrino mass. In the standard PDG parametrization, $\langle m_{ee} \rangle$ is expressed as,

$$\langle m_{ee} \rangle \equiv \left| \sum_j U_{ej}^2 m_j \right| = |c_{12}^2 c_{13}^2 m_1 e^{-2i\phi_1} + s_{12}^2 c_{13}^2 m_2 e^{-2i\phi_2} + s_{13}^2 m_3 e^{2i\delta_{\text{CP}}}|. \quad (31)$$

where, $c_{ij} = \cos \theta_{ij}$, $s_{ij} = \sin \theta_{ij}$, and m_i are neutrino masses, ϕ_1, ϕ_2 are Majorana CP phases while δ_{CP} is the Dirac CP phase. The current limits on $0\nu\beta\beta$ decays from KamLAND-Zen [52], EXO [53], GERDA Phase-II [54], and CUORE [55] experiments can be used to put constraints on $\langle m_{ee} \rangle$.

The constrained values of the CP phases and masses in our model imply that the value of $\langle m_{ee} \rangle$ is strongly constrained as shown by the blue and green regions in the left panel of Fig. 5. The color code remains the same as in the previous plots. Again the splitting between green and blue points is due to the non-fulfillment of 3σ constraints of either the mixing angles or the two mass-squared differences. The orange region represents the full model-independent parameter space allowed by the latest global-fit data [7]. The vertical gray band shows the constraint on the light neutrino mass arising from the *Planck* (TT, TE, EE + lowE + lensing + BAO) dataset, which has set an upper bound

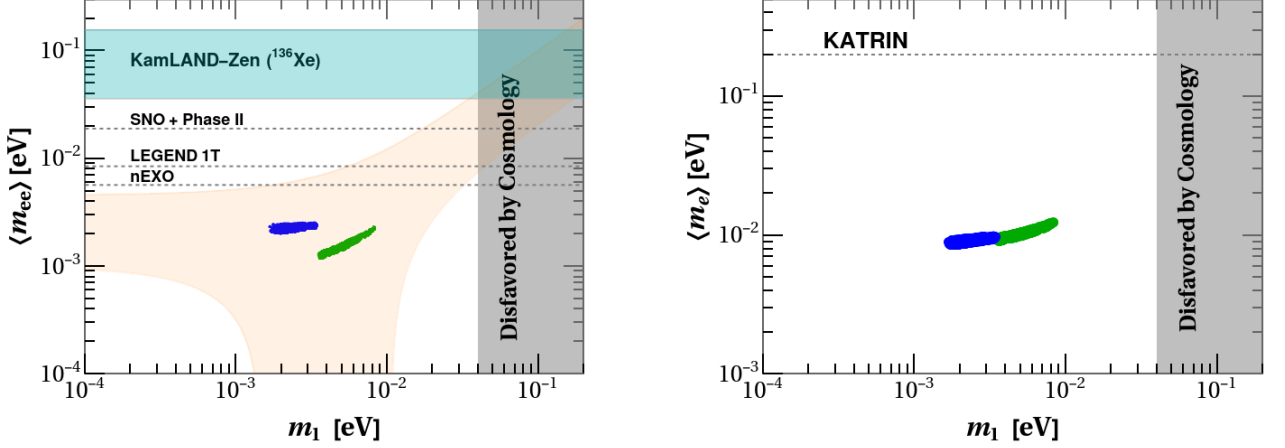


FIG. 5: **Left:** The effective Majorana neutrino mass $\langle m_{ee} \rangle$, **Right:** the effective mass of the electron neutrino $\langle m_e \rangle$, as a function of the lightest neutrino mass are shown. The green (blue) color region shows our model predictions whereas the orange region in the left panel shows the parameter space allowed by current oscillation data for NO. See text for more details.

on the sum of neutrino masses $\sum m_i < 0.12$ eV [9]. The horizontal cyan band indicates the current experimental limits from KamLAND-Zen ([36–156] meV) [52], while the black-dashed lines correspond to the projected sensitivities for SNO+ Phase II ([19 – 46] meV) [56], LEGEND 1000 ([8.5 – 19.4] meV) [57], nEXO ([5.7 – 17.7] meV) [58] at 90% C.L.. One could see that the model predictions remain outside the testable range of the next generation $0\nu\beta\beta$ decay experiments. Thus, any observation of $0\nu\beta\beta$ decay by these experiments will completely rule out our model.

In the right panel of Fig. 5, we have shown our model prediction for the effective mass of the electron neutrino $\langle m_e \rangle$, defined as

$$\langle m_e \rangle \equiv \sqrt{\sum_j |U_{ej}|^2 m_j^2} = \sqrt{c_{12}^2 c_{13}^2 m_1^2 + s_{12}^2 c_{13}^2 m_2^2 + s_{13}^2 m_3^2}. \quad (32)$$

The horizontal dashed line in the right panel of Fig. 5 corresponds to the expected full dataset sensitivity of KATRIN [59] ($\langle m_e \rangle < 0.2$ eV) while the vertical gray line corresponds to the Planck limit. Thus a measurement of $\langle m_e \rangle$ by KATRIN can also completely rule out our model.

4. DARK SECTOR

We now come to the dark sector predictions of our model. To start with, recall that in the canonical scotogenic model [10], the lightest \mathbb{Z}_2 odd particle (among scalar η and fermions N) running inside the loop, plays the role of a possible DM candidate. Depending on the masses of the dark sector particles, one ends up with two possible DM candidates: the lightest neutral dark scalar or the lightest dark fermion.

In our case, after $A_4 \rightarrow \mathcal{Z}_2$ breaking, the components of A_4 triplets η and N fields transform under the residual \mathcal{Z}_2 symmetry as follows (see Appendix A 1):

$$\begin{aligned} N_1 &\rightarrow +N_1, & \eta_1 &\rightarrow +\eta_1, \\ N_{2,3} &\rightarrow -N_{2,3}, & \eta_{2,3} &\rightarrow -\eta_{2,3}. \end{aligned} \quad (33)$$

All the remaining SM fields are even under \mathcal{Z}_2 as they are singlets of A_4 . Thus the dark sector in our model consists of the \mathcal{Z}_2 odd particles η_2 , η_3 , N_2 and N_3 with the lightest electrically neutral particle being the DM candidate.

As discussed in Sec. 2.2.1, masses of scalars have an upper bound ~ 600 GeV. The lower value of fermion mass ($\lesssim 600$ GeV) is not in good agreement with the two mass-squared differences (Δm_{atm}^2 and Δm_{sol}^2) of neutrino oscillations, as presented in Appendix B. Therefore, in this model, the only viable option for DM is a scalar particle. In what follows, we present a comprehensive analysis of scalar DM.

4.1. Scalar dark matter

In the scalar sector the $SU(2)_L$ doublets η_2 and η_3 are odd under \mathcal{Z}_2 and their neutral components can be a DM candidate. From Eq. (6), it is evident that after SSB we have four neutral dark scalars, namely η_2^R , η_2^I , η_3^R and η_3^I . In principle, out of these four scalars, anyone can be the lightest and can serve as a DM candidate. For the sake of definiteness throughout this section we take η_2^R as a scalar DM candidate with the following condition:

$$m_{\eta_2^R} < m_{\eta_2^I}, m_{\eta_3^R}, m_{\eta_3^I}. \quad (34)$$

Note that taking another one of them as a DM candidate will not change the main results of our analysis. We have performed a detailed numerical scan for the model parameters taking into account the various experimental and theoretical constraints. To generate the allowed points, we have imposed the following conditions:

- The tree-level vacuum stability has been imposed in accordance with Eq. (5).
- The positivity of pseudo scalar (A) and charged Higgs (H^\pm) mass, have been ensured by taking $\lambda_{11} < 0$ and $\lambda_{10} + 2\lambda_{11} < 0$ respectively, see Eq. (12).
- $\lambda_{12,13,14,15} > 0$ has been chosen to ensure the $m_{\eta_2^R} < m_{\eta_3^R}$.
- In addition, we have also imposed the condition $m_{\eta_2^R} < m_{\eta_2^I}$ (the condition $\lambda_{12,13,14,15} > 0$, automatically ensures that $m_{\eta_2^R} < m_{\eta_3^I}$).
- Note that these constraints automatically satisfy the condition mentioned in Eq. (34).

- The remaining couplings are allowed to vary freely following the Eq. (12).
- The fermion mass M and Yukawa couplings y_i are varied in the range given in Table II, always ensuring that the neutrino sector observables are within their 3σ range.
- The input parameters for scalar sector analysis are taken in the ranges provided in Table. II.

Relic density

We start with the computation of the relic abundance for η_2^R as DM. In Fig. 6, we show our result for relic density as a function of the mass of the scalar DM η_2^R . The numerical scan is performed by varying the input parameters as given in Table II and applying the constraints mentioned before. The narrow band shown by black dotted lines corresponds to the 3σ range for the cold DM relic density reported by the Planck satellite data [9]:

$$0.1126 \leq \Omega_{\eta_2^R} h^2 \leq 0.1246 .$$

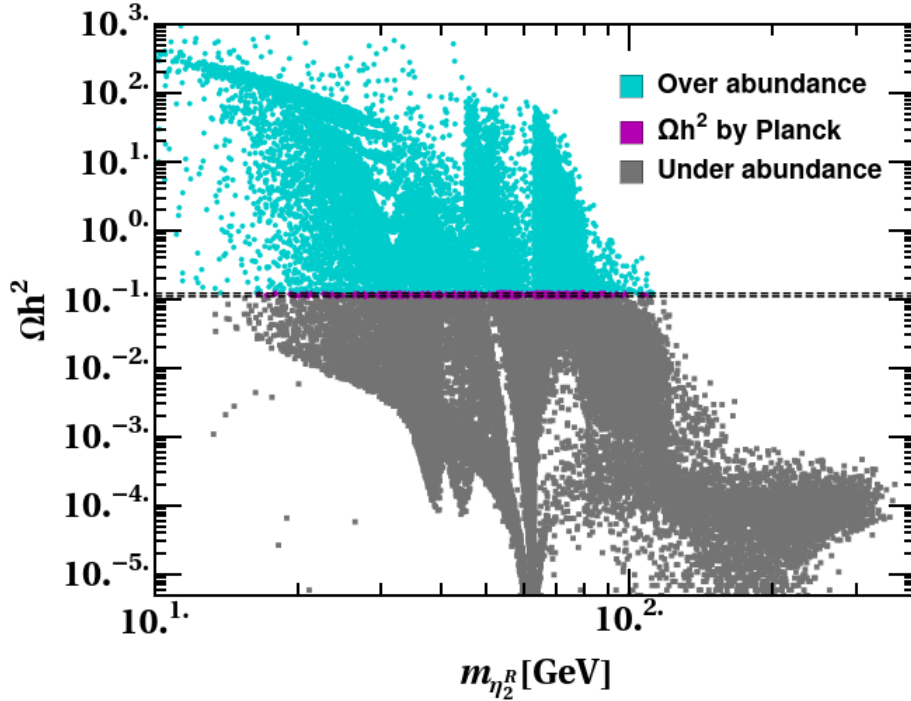


FIG. 6: Relic density as a function of scalar DM mass $m_{\eta_2^R}$. The cyan, magenta, and gray points depict over, observed, and under abundance of the DM relic density, respectively. The horizontal black dashed lines signify the latest Planck satellite data [9].

The points that lie within this narrow band correspond to η_2^R as 100% DM candidate. These points are shown in magenta color in Fig. 6. While the cyan/gray color points represent over/under abundance of relic density, respectively. There are three sharp dips in Fig. 6. The first dip is at $m_{\eta_2^R} \sim M_W/2$, the second dip is at $m_{\eta_2^R} \sim M_Z/2$ and third dip is at $m_{\eta_2^R} \sim m_{H_1}/2$, which corresponds to annihilation via s-channel W boson exchange, Z boson exchange, and Higgs boson exchange, respectively as shown in Fig. 10 in Appendix D 1. Also, one can notice that the dip at $m_{\eta_2^R} \sim m_{H_1}/2$ is more efficient as compared to dips at $M_W/2$ and $M_Z/2$. This is because couplings corresponding to Higgs channels are much stronger (being proportional to $\lambda_i v_1$) than the gauge couplings of the W and Z channel annihilations.

Furthermore, as shown in Fig. 6, the correct relic density points (depicted in magenta) are confined to the parameter space where $m_{\eta_2^R} \lesssim 100$ GeV. Beyond this region (i.e. $m_{\eta_2^R} > 100$ GeV), there are no data points corresponding to correct relic abundance. In the latter region, the relic density is under abundant. This occurs because once the A_4 symmetry is broken by $\langle \eta_1 \rangle = v_2/\sqrt{2}$, the mass parameter μ_η^2 in Eq. (1) is no longer free parameter, instead, it depends on quartic couplings λ_s , see Eq. (12). Thus, achieving a higher mass value for η_2^R is possible only by increasing the λ_s . However, the larger the value of λ_s (and hence $m_{\eta_2^R}$), the larger the cross-section of DM annihilation to SM particles. Consequently, the value of relic density will decrease, and beyond $m_{\eta_2^R} \lesssim 100$ GeV, DM is always under abundant. Finally, apart from satisfying the relic abundance, a good candidate for DM should also satisfy various experimental constraints including the collider and direct detection constraints which we discuss in the next section.

Collider and Direct detection constraints

This section discusses the collider and direct detection (DD) experimental constraints for the DM candidate η_2^R . The collider constraints namely, LEP (LEP-I, LEP-II) and LHC have a significant impact on the viable parameter space of the DM mass. The LEP constraints impose lower bounds on the masses of dark sector scalar particles, with the most stringent ones being:

- *The LEP-I measurements rule out SM-gauge boson decays into dark sector particles [60, 61]. This condition leads to the following lower limit on the dark sector scalar masses:*

$$m_{\eta_{2/3}^{R/I}} + m_{\eta_{2/3}^\pm} > M_W, \quad m_{\eta_{2/3}^R} + m_{\eta_{2/3}^I} > M_Z, \quad m_{\eta_{2/3}^\pm} + m_{\eta_{2/3}^\mp} > M_Z. \quad (35)$$

- *Chargino searches in LEP-II in context of singly-charged scalar production $e^+e^- \rightarrow h^+h^-$ can be adapted to our analysis to set the limits [62] given by*

$$m_{\eta_{2/3}^\pm} > 70 \text{ GeV}. \quad (36)$$

The most important LHC limit comes from the possibility of Higgs “invisible decay” to dark sector particles. The Higgs invisible decay comes through the channel $H_1 \rightarrow \eta_{2/3}^{R/I} \eta_{2/3}^{R/I}$. The current bound for the branching ratio of Higgs invisible from LHC data has limit [63]:

$$BR(H_1 \rightarrow inv) < 0.145. \quad (37)$$

Apart from collider constraints, the DM parameter space is also constrained by limits from DD experiments. In our model the tree-level spin-independent η_2^R -nucleon cross section is mediated by

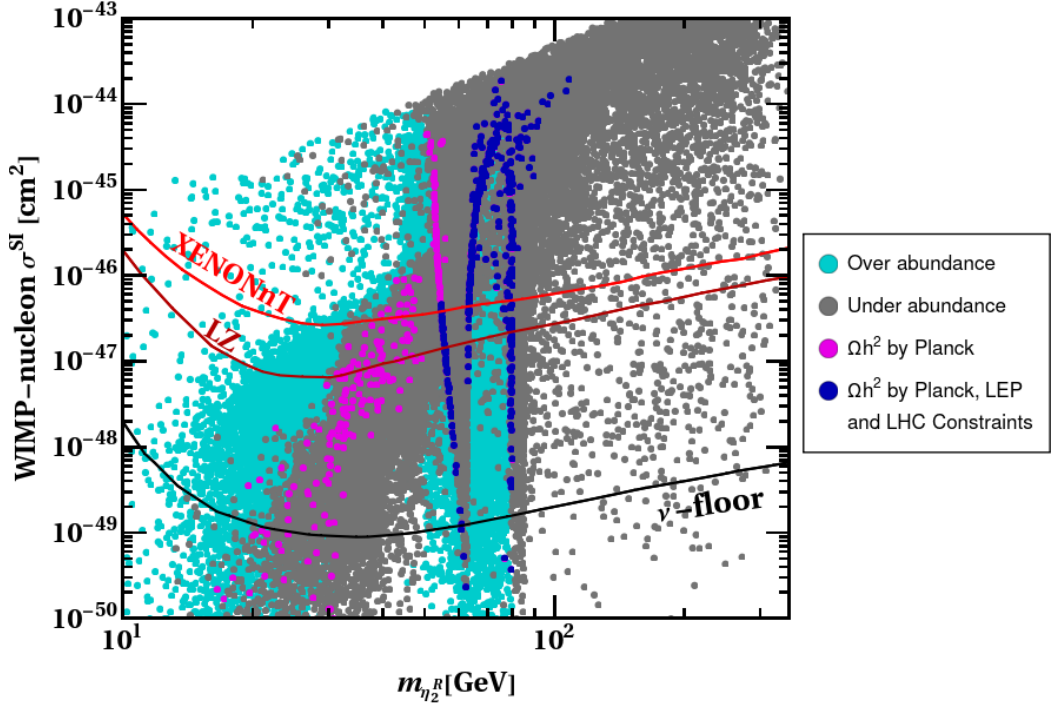


FIG. 7: Spin-independent WIMP-nucleon cross section for the scalar DM.

the Higgs (H_1) and the Z-portals as shown in Fig. 13 in Appendix D 1. Note that, like the canonical scotogenic model, here also the Higgs portal dominates and the contribution through the Z-portal can be neglected when compared to the Higgs portal. We have shown our result for direct detection of the scalar DM candidate η_2^R in Fig. 7, varying the input parameters as given in Table II. For consistency, we utilize the same color code used in Fig. 6 with cyan, magenta, and gray points representing over, correct, and under abundant relic density, respectively. The blue color points in Fig. 7 represent the correct relic density points which also satisfies the collider constraints mentioned in Eqs. (35), (36), (37) by LEP (LEP-I, LEP-II), and LHC.

The red and dark red line in Fig. 7 denotes the latest DD upper bounds from the XENONnT collaboration [64] and LZ collaboration [65], respectively. The black line represents the lower limit

corresponding to the “neutrino floor” from coherent elastic neutrino scattering [66]. From Fig. 7, one can infer that the blue points that lie below the LZ limit are allowed points satisfying the relic density, LEP, LHC and DD constraints. This allowed region is from 55 GeV to 80 GeV. Thus, our model is compatible with all the constraints within the DM mass range of $55 \text{ GeV} \leq m_{\eta_2^R} \leq 80 \text{ GeV}$.

5. CONCLUSIONS

In this work, we have proposed a novel framework where tiny neutrino masses, the two observed mass scales in neutrino oscillation experiments, the leptonic flavor structure, and dark matter can be explained using a single flavor symmetry. We have demonstrated the framework by explicitly constructing a simple model using the A_4 flavor symmetry. The model extends the SM by introducing scalars and fermions that transform as triplets under the A_4 symmetry. We show that the spontaneous breaking of A_4 symmetry to its \mathcal{Z}_2 subgroup leads to a scoto-seesaw hybrid mass mechanism in the neutrino sector, where an interplay between the tree-level type-I seesaw and the one-loop level scotogenic mechanism generates neutrino masses. Furthermore, the residual \mathcal{Z}_2 acts as a scotogenic dark symmetry that stabilizes the DM.

After conducting numerical analysis, we find that the model aligns with the normal neutrino mass ordering and predicts a small range along with a lower bound on the lightest neutrino mass. The predicted flavor mixing patterns exhibit a generalized $\mu - \tau$ reflection symmetric flavor structure, consistent with the latest neutrino oscillation data, with δ_{CP} phase close to 1.5π value. We also discuss the predictions of our model for the neutrinoless double beta decay and beta decay experiments. The results are summarized in Figs. 3 - 5.

For the dark sector, we show that the experimental constraints coming from neutrino oscillation data rule out the possibility of having fermionic DM, a reflection of the flavor origin of the dark sector. For the scalar DM case, the higher mass region is not allowed due to the perturbativity limit of scalar couplings. The observed DM relic abundance can be only explained for the lower mass region $m_{\eta_2^R} \leq 100 \text{ GeV}$ (see Fig. 6). Further, the imposition of LEP, LHC, and direct detection constraints makes the allowed parameter space for DM mass to be in the $55 \text{ GeV} \leq m_{\eta_2^R} \leq 80 \text{ GeV}$ range. In summary, our explicit model is highly predictive with its predictions testable in various neutrino sectors as well as dark matter experiments.

Before ending, we want to emphasize that the model presented in this work serves as a specific example of a broader framework, where an appropriate flavor symmetry with proper residual subgroup can be used to achieve similar results. Thus, various extensions and generalizations of this model are possible. For example, even with A_4 symmetry, this idea can be generalized using a different set of BSM particles and/or assigning the particles the A_4 representations in a different way or by using different one or higher loop neutrino mass models. One can also use other flavor symmetries whose subgroups

potentially can stabilize the DM candidate. We plan to discuss some of these possibilities in future works.

6. ACKNOWLEDGEMENTS

Authors would like to acknowledge the MPT [67], SARAH [68], SPheno [69] and micrOMEGAS [70] packages which have been used to perform the numerical analysis. RK acknowledges the funding support by the CSIR SRF-NET fellowship. NN is supported by the Spanish grants PID2020-113775GB-I00 (AEI/10.13039/501100011033) and Prometeo CIPROM/2021/054 (Generalitat Valenciana). NN also acknowledges the Istituto Nazionale di Fisica Nucleare (INFN) through the ‘‘Theoretical Astroparticle Physics’’ (TAsP) project. The work of RS is supported by SERB, Government of India grant SRG/2020/002303.

RS would like to dedicate this work to his newborn daughter Akanksha whose gestation took less than half the gestation time of this work.

Appendix A: A_4 symmetry and scalar potential

1. Transformation rules for A_4 symmetry and its Z_2 subgroup

The A_4 symmetry is a non-abelian discrete flavor group. It is an even permutation group of four objects. It is also the symmetry group of a regular tetrahedron. It has 12 elements and can be generated by two generators S and T obeying the relations:

$$S^2 = T^3 = (ST)^3 = I. \quad (A1)$$

In the basis where S and T are real matrices, the generators are given by,

$$S = \begin{pmatrix} 1 & 0 & 0 \\ 0 & -1 & 0 \\ 0 & 0 & -1 \end{pmatrix}, \quad T = \begin{pmatrix} 0 & 1 & 0 \\ 0 & 0 & 1 \\ 1 & 0 & 0 \end{pmatrix}. \quad (A2)$$

A_4 has four irreducible representations, three of them are one-dimensional (i.e. three singlets) 1, $1'$, and $1''$, and one of them is three-dimensional (triplet) 3. The multiplication rule for these representations are:

$$\begin{aligned} 1 \times 1 &= 1 = 1' \times 1'', & 1' \times 1' &= 1'', & 1'' \times 1'' &= 1', \\ 1 \times 3 &= 3, & 3 \times 3 &= 1 + 1' + 1'' + 3_1 + 3_2. \end{aligned} \quad (A3)$$

where 3_1 and 3_2 denote the two different ways the components of the triplets can be multiplied. If $a = (a_1, a_2, a_3)$ and $b = (b_1, b_2, b_3)$ are two triplets then their multiplication rules are given as follows [71]:

$$\begin{aligned}
(ab)_1 &= a_1b_1 + a_2b_2 + a_3b_3, \\
(ab)_{1'} &= a_1b_1 + \omega a_2b_2 + \omega^2 a_3b_3, \\
(ab)_{1''} &= a_1b_1 + \omega^2 a_2b_2 + \omega a_3b_3, \\
(ab)_{3_1} &= (a_2b_3, a_3b_1, a_1b_2), \\
(ab)_{3_2} &= (a_3b_2, a_1b_3, a_2b_1),
\end{aligned} \tag{A4}$$

where ω is the cubic root of unity.

The A_4 group has a \mathcal{Z}_2 subgroup as mentioned before. If the A_4 group is broken spontaneously by VEV of a triplet scalar φ with VEV alignment $\langle \varphi \rangle \sim \frac{1}{\sqrt{2}}(v, 0, 0)$, then the \mathcal{Z}_2 group remains unbroken [42]. This happens because the generator S remains invariant i.e.

$$S\langle \varphi \rangle \equiv \begin{pmatrix} 1 & 0 & 0 \\ 0 & -1 & 0 \\ 0 & 0 & -1 \end{pmatrix} \begin{pmatrix} \frac{v}{\sqrt{2}} \\ 0 \\ 0 \end{pmatrix} = \begin{pmatrix} \frac{v}{\sqrt{2}} \\ 0 \\ 0 \end{pmatrix} \equiv \langle \varphi \rangle. \tag{A5}$$

leaving the \mathcal{Z}_2 subgroup unbroken.

In such a case any other field transforming as one of the singlets of A_4 will be even (+) under the residual \mathcal{Z}_2 subgroup. For a triplet of A_4 , $\Psi \equiv (a_1, a_2, a_3)^T$, under S transformation we have:

$$S\Psi = \begin{pmatrix} 1 & 0 & 0 \\ 0 & -1 & 0 \\ 0 & 0 & -1 \end{pmatrix} \begin{pmatrix} a_1 \\ a_2 \\ a_3 \end{pmatrix} = \begin{pmatrix} a_1 \\ -a_2 \\ -a_3 \end{pmatrix} \tag{A6}$$

This means that after $A_4 \rightarrow \mathcal{Z}_2$, the first component of the triplet field Ψ transforms as even (+) under \mathcal{Z}_2 while the other two components transform as odd (−) under \mathcal{Z}_2 . This fact is crucial to our work.

In our model, we have two triplets N and η . Once A_4 symmetry is broken, the transformation of their components under the \mathcal{Z}_2 residual symmetry is given by:

$$\begin{aligned}
N_1 &\rightarrow +N_1, & \eta_1 &\rightarrow +\eta_1, \\
N_{2,3} &\rightarrow -N_{2,3}, & \eta_{2,3} &\rightarrow -\eta_{2,3}.
\end{aligned} \tag{A7}$$

The remaining fields are all \mathcal{Z}_2 even, because they are singlets of A_4 . Thus after $A_4 \rightarrow \mathcal{Z}_2$ symmetry breaking, the particles running inside the loop all have \mathcal{Z}_2 odd charges while all SM particles are \mathcal{Z}_2 even. This allows us to use the unbroken \mathcal{Z}_2 subgroup as the dark symmetry of the scotogenic model.

2. Scalar Potential

Now moving to the scalar potential, we have two scalars Φ and η , singlet and triplet of A_4 respectively. The $SU(3)_C \otimes SU(2)_L \otimes U(1)_Y \otimes A_4$ invariant scalar potential can be written as:

$$\begin{aligned}
V = & \mu_\Phi^2 \Phi^\dagger \Phi + \mu_\eta^2 [\eta^\dagger \eta]_1 + \lambda_1 (\Phi^\dagger \Phi)^2 + \lambda_2 [\eta^\dagger \eta]_1^2 + \lambda_3 [\eta^\dagger \eta]_{1'} [\eta^\dagger \eta]_{1''} + \lambda_4 [\eta^\dagger \eta]_{1'} [\eta \eta]_{1''} \\
& + \lambda_{4'} [\eta^\dagger \eta]_{1''} [\eta \eta]_{1'} + \lambda_5 [\eta^\dagger \eta]_1 [\eta \eta]_1 + \lambda_6 \left([\eta^\dagger \eta]_{3_1} [\eta^\dagger \eta]_{3_1} + h.c. \right) + \lambda_7 [\eta^\dagger \eta]_{3_1} [\eta^\dagger \eta]_{3_2} \\
& + \lambda_8 [\eta^\dagger \eta]_{3_1} [\eta \eta]_{3_2} + \lambda_9 [\eta^\dagger \eta]_1 (\Phi^\dagger \Phi) + \lambda_{10} [\eta^\dagger \Phi]_3 [\Phi^\dagger \eta]_3 + \lambda_{11} \left([\eta^\dagger \eta]_1 \Phi \Phi + h.c. \right) \\
& + \lambda_{12} \left([\eta^\dagger \eta]_{3_1} [\eta \Phi]_3 + h.c. \right) + \lambda_{13} \left([\eta^\dagger \eta]_{3_2} [\eta \Phi]_3 + h.c. \right) + \lambda_{14} \left([\eta^\dagger \eta]_{3_1} [\eta^\dagger \Phi]_3 + h.c. \right) \\
& + \lambda_{15} \left([\eta^\dagger \eta]_{3_2} [\eta^\dagger \Phi]_3 + h.c. \right), \tag{A8}
\end{aligned}$$

where $[\dots]_p$; $p = 1, 1', 1'', 3, 3_1, 3_2$ denote the A_4 transformation of enclosed fields.

To see how many independent λ 's appear in the potential, we expand terms in their A_4 components. Upon expanding, it becomes evident that certain terms are common across different couplings, allowing us to combine them as written in Eq. (A9). This can be understood from the $A_4 \otimes SU(2)_L$ group multiplication. The number of invariants under $A_4 \otimes SU(2)_L$ is determined by the following multiplication:

$$(\eta \eta) \sim (3, 2) \times (3, 2) = (1 + 1' + 1'' + 3_1, 3) + (3_2, 1).$$

As a result, we end up with five independent invariants of the type $(\eta^\dagger \eta) (\eta^\dagger \eta)$ [46]. Also, there are four invariants of the type $(\eta^\dagger \eta) (\Phi^\dagger \Phi)$ or $(\eta^\dagger \Phi)^2$ and two of $(\eta^\dagger \eta) (\eta^\dagger \Phi)$ type, as given in Eq. (A9).

The potential is CP conserving if all couplings are taken to be real and $\lambda_{4'} = \lambda_4$. This can be written in combined form as

$$\begin{aligned}
V = & \mu_\Phi^2 \Phi^\dagger \Phi + \mu_\eta^2 \left(\eta_1^\dagger \eta_1 + \eta_2^\dagger \eta_2 + \eta_3^\dagger \eta_3 \right) + \lambda_1 \left(\Phi^\dagger \Phi \right)^2 + \mathbf{\Lambda}_2 \left((\eta_1^\dagger \eta_1)^2 + (\eta_2^\dagger \eta_2)^2 + (\eta_3^\dagger \eta_3)^2 \right) \\
& + \mathbf{\Lambda}_3 \left[\left(\eta_1^\dagger \eta_1 \right) \left(\eta_2^\dagger \eta_2 \right) + \left(\eta_2^\dagger \eta_2 \right) \left(\eta_3^\dagger \eta_3 \right) + \left(\eta_3^\dagger \eta_3 \right) \left(\eta_1^\dagger \eta_1 \right) \right] + \mathbf{\Lambda}_4 \left[\left(\eta_1^\dagger \eta_2 \right)^2 + \left(\eta_2^\dagger \eta_3 \right)^2 + \left(\eta_3^\dagger \eta_1 \right)^2 + h.c. \right] \\
& + \lambda_7 \left[\left(\eta_2^\dagger \eta_3 \right) \left(\eta_3^\dagger \eta_2 \right) + \left(\eta_3^\dagger \eta_1 \right) \left(\eta_1^\dagger \eta_3 \right) + \left(\eta_1^\dagger \eta_2 \right) \left(\eta_2^\dagger \eta_1 \right) \right] + \lambda_9 \left(\eta_1^\dagger \eta_1 + \eta_2^\dagger \eta_2 + \eta_3^\dagger \eta_3 \right) \left(\Phi^\dagger \Phi \right) \\
& + \lambda_{10} \left[\left(\eta_1^\dagger \Phi \right) \left(\Phi^\dagger \eta_1 \right) + \left(\eta_2^\dagger \Phi \right) \left(\Phi^\dagger \eta_2 \right) + \left(\eta_3^\dagger \Phi \right) \left(\Phi^\dagger \eta_3 \right) \right] + \lambda_{11} \left[\left(\eta_1^\dagger \Phi \right)^2 + \left(\eta_2^\dagger \Phi \right)^2 + \left(\eta_3^\dagger \Phi \right)^2 + h.c. \right] \\
& + \mathbf{\Lambda}_{12} \left[\left(\eta_3^\dagger \eta_1 \right) \left(\eta_2^\dagger \Phi \right) + \left(\eta_1^\dagger \eta_2 \right) \left(\eta_3^\dagger \Phi \right) + \left(\eta_2^\dagger \eta_3 \right) \left(\eta_1^\dagger \Phi \right) + h.c. \right] \\
& + \mathbf{\Lambda}_{13} \left[\left(\eta_2^\dagger \eta_1 \right) \left(\eta_3^\dagger \Phi \right) + \left(\eta_3^\dagger \eta_2 \right) \left(\eta_1^\dagger \Phi \right) + \left(\eta_1^\dagger \eta_3 \right) \left(\eta_2^\dagger \Phi \right) + h.c. \right]. \tag{A9}
\end{aligned}$$

where $\mathbf{\Lambda}_2 = (\lambda_2 + \lambda_3 + 2\lambda_4 + \lambda_5) \equiv \Lambda$ (see Eq.(7)), $\mathbf{\Lambda}_3 = (2\lambda_2 - \lambda_3 + \lambda_8)$, $\mathbf{\Lambda}_4 = (\lambda_5 + \lambda_6 - \lambda_4)$, $\mathbf{\Lambda}_{12} = (\lambda_{12} + \lambda_{14})$, and $\mathbf{\Lambda}_{13} = (\lambda_{13} + \lambda_{15})$.

Furthermore, the potential of Eq. (A9) can be simplified in $SU(2)_L$ components and the mass spectrum of scalars can be computed as discussed in Sec. 2.2.2.

Appendix B: Fermionic dark matter

As we have already discussed in Sec. 2.2.1, in our models all the scalar masses have an upper bound $\lesssim 600$ GeV. For a dark sector particle to be a good DM candidate its mass has to be less than the other dark sector particles. Therefore, even fermionic DM candidates in our model should have masses $\lesssim 600$ GeV. Here, we have two potential fermionic DM candidates N_2 and N_3 which are odd under \mathcal{Z}_2 and are nearly mass degenerate. For the sake of definiteness, we have chosen N_2 as the lightest dark sector particle and hence a potential DM candidate with the following conditions:

$$M_2 \leq M_3, m_{\eta_2^R}, m_{\eta_3^R}, m_{\eta_2^I}, m_{\eta_3^I}, m_{\eta_2^\pm}, m_{\eta_3^\pm} \lesssim 600 \text{ GeV}. \quad (\text{B1})$$

Choosing N_3 as a DM candidate will imply $M_3 \leq M_2$ but will not change any of the salient points of the analysis. The numerical analysis has been done following the Table III and Eq. (B1).

Parameters	Range	Parameters	Range
λ_1	$[10^{-3}, \sqrt{4\pi}]$	$\lambda_{12,13,14,15}$	$[10^{-8}, 10^{-2}]$
$ \lambda_{2,3,\dots,10} $	$[10^{-6}, \sqrt{4\pi}]$	$M_{1,2,3}$ (in GeV)	$[10, 600]$
λ_{11}	$-[10^{-6}, \sqrt{4\pi}]$	y_i	$[10^{-8}, 10^{-6}]$

TABLE III: Value range for the numerical parameter scan in the dark sector for fermionic DM.

Relic density

We show our results for DM relic density (Ωh^2) as a function of the fermionic DM mass M_2 in Fig. 8. The correct relic density can be obtained for the N_2 mass as heavy as ≈ 400 GeV. In the left panel of Fig. 8 we have shown correct relic density points in magenta color along with the over abundant and under abundant points shown in cyan and gray colors respectively. The right panel of Fig. 8 illustrates the behavior of relic density based on the mass difference of N_2 and the lightest dark sector scalar η_2^R . One can notice that for large mass difference $m_{\eta_2^R} - M_2 = \Delta m \sim 60$ GeV most of the points (yellow color points in the right panel of Fig. 8) are over abundant. This pattern of relic density is due to the different annihilation and co-annihilation modes of the N_2 , see Appendix D 2.

Annihilation and co-annihilation channels which determine the observed DM relic density are given in Appendix D 2 in Figs. 14, 15, 16 and 17. When the masses of dark sector scalars η_2 and η_3 significantly exceed that of the DM candidate N_2 , only annihilation (co-annihilation) channel $N_2 N_{2/3} \rightarrow l_i^\mp l_j^\pm, \nu_i \nu_j$ play significant role in the relic density computation. These interactions are mediated by the heavy dark sector scalars, resulting in relatively small cross sections. The consequence of these small cross sections is a high relic density, leading to an over abundance of DM in most cases where there is a

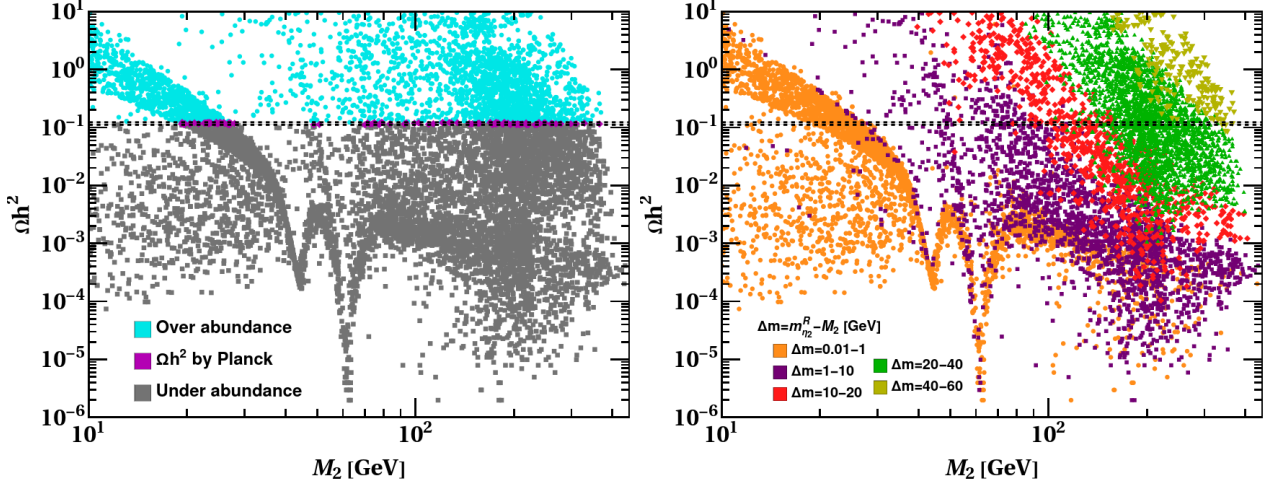


FIG. 8: Relic density as a function of fermionic DM mass M_2 has been presented in both panels. In the left panel, cyan, magenta, and gray points depict over, observed, and under abundance of the DM relic density, respectively. The narrow band signifies the latest Planck satellite data [9]. The same has been shown in the right panel, where the behavior of relic density has been shown with respect to the mass difference between the lightest dark sector scalar and fermionic DM (i.e., $\Delta m = m_{\eta_2^R} - M_2$) using the orange, purple, red, green, and yellow points, where values of Δm are marked in the plot. See the main text for detailed discussion.

significant mass difference. While it is possible to enhance these cross sections a bit by considering large Yukawa couplings (y_i), it is worth noting that Yukawa couplings (y_i) are also bounded by their perturbativity limits as well as by the requirement of obtaining small masses for neutrinos. Thus for larger Δm correct relic density cannot be obtained for any value of the Yukawa couplings. Changing the mass differences between other dark sector scalars (besides η_2^R) and N_2 also does not help and the conclusion will remain the same.

In scenarios marked by low mass differences between dark sector scalars and DM candidates, additional annihilation and co-annihilation channels become significant along with the $N_2 N_{2/3} \rightarrow l_i^\mp l_j^\pm, \nu_i \nu_j$ channels. When the mass difference, denoted as Δm , is relatively small, all these annihilation and co-annihilation channels shown in Figs. 14, 15, 16, 17 contribute significantly, leading to a higher cross section compared to scenarios with large Δm . In the latter case, the primary contribution arises solely from the $N_2 N_{2/3} \rightarrow l_i^\mp l_j^\pm, \nu_i \nu_j$ channel. This enhancement in the cross section for small mass differences results in lower relic density values as well as correct relic density as shown in the right panel of Fig. 8. For mass differences $\Delta m \leq 40$ GeV, a considerable number of data points fall inside the 3σ range for the DM relic density reported by the Planck satellite data [9].

Direct detection

Here, we will briefly discuss the direct detection process for fermionic DM case in our model. Notably, there exists no direct coupling between the fermionic DM N_2 and quarks. Hence, at the tree-level, no interaction occurs between N_2 and quarks. Nonetheless, at the one-loop level, N_2 can couple with quarks through Z boson, photon (γ), and Higgs boson (H_1) as depicted in Fig. 18 in Appendix D 2 leading to a non-zero DM-nucleon cross section.

The spin-dependent cross section per nucleon is given by the following expression [72].

$$\sigma_{SD} \sim 10^{-4} \text{pb} \left(\frac{y_i}{3}\right)^4 \mathcal{G}_2 \left(\frac{M_2^2}{m_\gamma^2}\right)^2$$

where, $\mathcal{G}_2(x)$ is loop function given in Ref. [72] and for our model it has value $\mathcal{G}_2 \left(\frac{M_2^2}{m_\gamma^2}\right)^2 \sim 1$.

The neutrino oscillation constraints imply⁵ that, for this case, all Yukawas in our model are of the order, $y_i \sim 10^{-8} - 10^{-6}$, see next section. Therefore,

$$\sigma_{SD} \sim 10^{-38} - 10^{-30} \text{pb.} \quad (\text{B2})$$

Also, the spin-independent cross section per nucleon, $\sigma_{SI} \propto y_i^4$ as discussed in [72]. Hence, σ_{SI} will also be equally small.

Given that direct detection in our model is only possible at the one-loop level and taking into account the small Yukawa couplings ($y_i \sim 10^{-8} - 10^{-6}$), the resulting spin-dependent (independent) cross section σ_{SD} (σ_{SI}) is exceedingly tiny. Consequently, this tiny cross section trivially satisfies the constraints from the direct detection experiments [64, 65].

Neutrino oscillations constraints for fermionic DM

Although fermionic DM satisfies all DM constraints, this scenario is not compatible with the neutrino oscillation data. As discussed previously, the dark Z_2 symmetry in our model emerges from the breaking of the A_4 symmetry. Thus the neutrino and dark sectors are intimately tied together with the same dark sector particles and Yukawa couplings playing important roles in both sectors. Furthermore, the scalar masses have an upper bound (~ 600 GeV), hence for N_2 to be fermionic DM, its mass has to be within this limit. In Fig. 9, we have shown that how Δm_{atm}^2 and Δm_{sol}^2 are related with each other. All points in Fig. 9 lie within the 3σ allowed range of mixing angles from global-fit data [7]. The band shown in cyan and magenta color depicts the 3σ allowed values of Δm_{atm}^2 and Δm_{sol}^2 respectively [7].

⁵ As discussed in the next section, the fermionic DM cannot simultaneously satisfy Δm_{atm}^2 and Δm_{sol}^2 constraints. We are taking Yukawas corresponding to the green points in the right panel of Fig. 9 which comes closest to simultaneously satisfying both mass square differences.

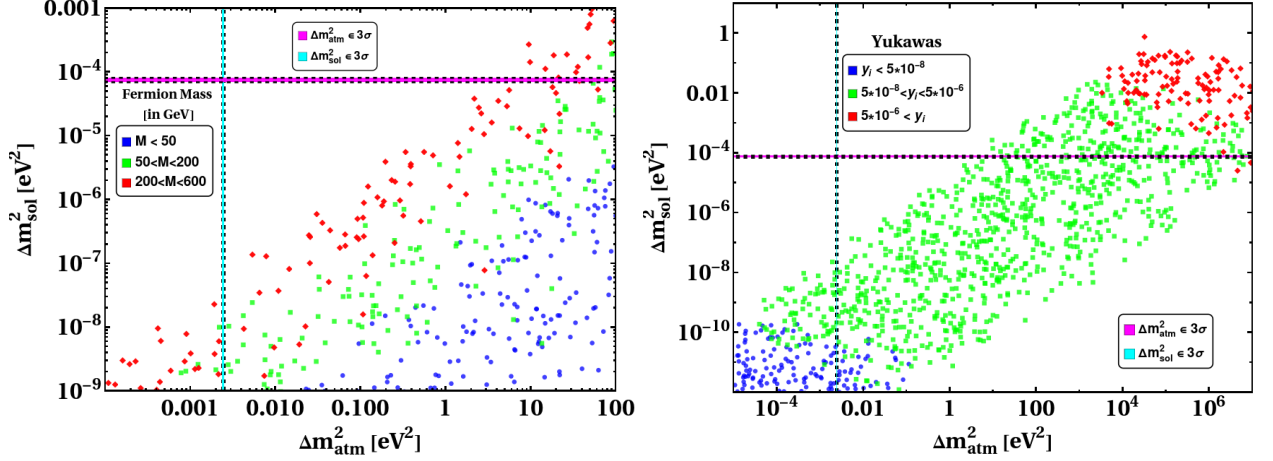


FIG. 9: Correlation between mass-squared differences (Δm_{atm}^2 and Δm_{sol}^2) of neutrino oscillation in fermionic DM case. **Left:** Correlation dependency on fermionic DM mass. **Right:** Correlation dependency on Yukawa couplings.

The left panel of Fig. 9 depicts the behavior of two mass-squared differences with the mass of fermionic DM. We notice that for lower values of fermionic DM mass, we can not satisfy any mass constraint while for higher values of fermionic DM mass, we can satisfy only one mass-squared constraint at a time. In the right panel of Fig. 9 we have shown the behavior of mass-squared differences in terms of Yukawa couplings. Hence, from Fig. 9 one can infer that within the allowed mass region of fermion N_2 (up to ~ 600 GeV), we are not able to simultaneously satisfy the two mass-squared differences Δm_{atm}^2 and Δm_{sol}^2 of neutrino oscillation. The results remain the same if N_3 is taken as the fermionic DM. In fact for any perturbative value of Yukawa couplings and masses of dark fermions $\leq 10^5$ GeV, the two oscillation length scales Δm_{atm}^2 and Δm_{sol}^2 cannot be simultaneously obtained within their respective experimental 3σ ranges. Thus, in our model, the neutrino oscillation constraints can only be satisfied for scalar DM.

This feature inherent to our model serves to distinguish it from conventional scotogenic as well as the scoto-seesaw models, where both scalar and fermionic DM are equally viable. Within the context of our model, the breaking of the A_4 symmetry plays a crucial role in having an upper bound on the scalar masses. Hence, for a stable fermionic DM, its mass has to be less than dark sector scalars. Within this limit of fermionic DM mass, the two mass scales of neutrino oscillation data can not be satisfied simultaneously. Therefore, the possibility of fermionic DM in our model is ruled out taking neutrino oscillations data into account. This outcome emphasizes the significance of A_4 flavor symmetry within our model, distinguishing it from the scotogenic and scoto-seesaw model and their variants. The utilization of this flavor symmetric approach yields unique implications for the DM candidate viability in our model, allowing only for the scalar DM.

Appendix C: Other possible representation of lepton doublets L_i under A_4

In this section, we discuss the other possible representations of A_4 for the lepton doublets L_i . In our current model we have assigned L_i to $(1, 1', 1'')$ charges under A_4 . The other possible scenarios for L_i are as follows

$$L_i \sim (1, 1'', 1'), (1', 1, 1''), (1'', 1, 1'), (1', 1'', 1), (1'', 1', 1) \quad (\text{C1})$$

To keep the charged lepton mass matrix diagonal, e_{R_i} should have the same representation as L_i . Since the singlets $1'$ and $1''$ of A_4 are conjugates of each other, only two distinct configurations, other than the one presented in the main text, are $(1', 1, 1'')$, $(1', 1'', 1)$. The final form of the light neutrino mass matrix for these two possibilities are:

- **II. For $L_i \sim (1', 1, 1'')$ case:** The final neutrino mass matrix from the tree and loop contribution has the following structure

$$m_\nu^{(II)} = \begin{pmatrix} y_1^2 (d_3 - z) & y_1 y_2 (d_2 - z) & y_1 y_3 (d_1 - z) \\ * & y_2^2 (d_1 - z) & y_2 y_3 (d_3 - z) \\ * & * & y_3^2 (d_2 - z) \end{pmatrix}. \quad (\text{C2})$$

- **III. For $L_i \sim (1', 1'', 1)$ case:** For this representation, the final neutrino mass matrix has the following structure

$$m_\nu^{(III)} = \begin{pmatrix} y_1^2 (d_3 - z) & y_1 y_2 (d_1 - z) & y_1 y_3 (d_2 - z) \\ * & y_2^2 (d_2 - z) & y_2 y_3 (d_3 - z) \\ * & * & y_3^2 (d_1 - z) \end{pmatrix}. \quad (\text{C3})$$

where $z = \frac{v_2^2}{2M}$ and d_i , ($i = 1, 2, 3$) are as defined in Eq. (26).

Here, we would like to mention that the structure of the matrices in Eqs. (C2) and (C3) differ significantly from the matrix in Eq. (27). A key distinction arises in the $y_2 = y_3$ limit, where matrix (27) resembles the exact $\mu - \tau$ reflection symmetry [39]. However, the alternative matrices in (C2) and (C3) fail to exhibit this structure under any particular limit. This highlights the importance of representation choice, contrary to the assertion in Ref. [44], where the results obtained by the authors are incorrect. We have analyzed the neutrino mass matrices provided in (C2) and (C3) numerically as well and found that indeed numerically as well their predictions differ from $L_i \sim (1, 1', 1'')$.

Appendix D: Feynman diagrams for relic density and direct detection

In this section, we show the possible Feynman diagrams that play a role in the determination of the relic density of DM for both scenarios, scalar DM η_2^R and fermionic DM N_2 . In addition, we have

included Feynman diagrams for direct detection of DM in both of these cases. The inclusion of these Feynman diagrams serves to assist our understanding of the dark sector results presented in Sec. 4 and in Appendix B.

1. Feynman diagrams for scalar DM

In Figs. 10, 11 and 12, we have shown possible Feynman diagrams corresponding to the annihilation and co-annihilation channels responsible for determining the relic density of scalar DM η_2^R . Fig. 10 illustrates the s-channel processes of DM annihilation and co-annihilation, mediated by the Higgs boson H_1 , W and Z bosons, along with other potential channels. On the other hand, Fig. 12 focuses on the annihilation of DM into gauge bosons through quartic couplings. In Fig. 13, we have shown the direct detection prospects of scalar DM η_2^R mediated by Higgs boson H_1 and Z boson.

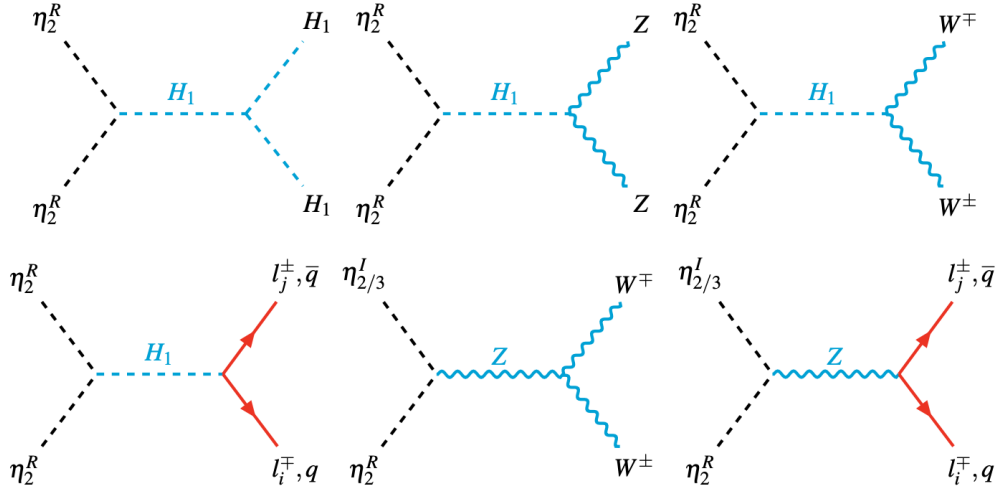


FIG. 10: Annihilation and co-annihilation channel for scalar DM η_2^R .

2. Feynman diagrams for fermionic DM

For the fermionic DM, the possible Feynman diagrams that govern the relic density are shown in Figs. 14, 15, 16 and 17. Furthermore, for the fermionic DM, we do not have tree-level interaction with quarks. Hence, Feynman diagrams for direct detection at the one-loop level are shown in Fig. 18.

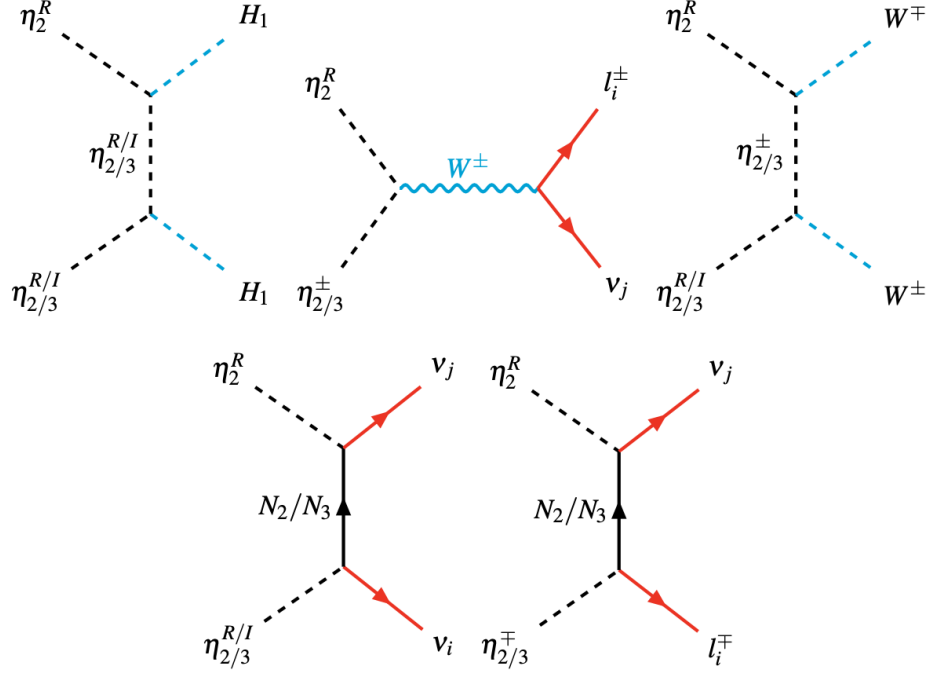


FIG. 11: Annihilation and co-annihilation channel for scalar DM η_2^R .

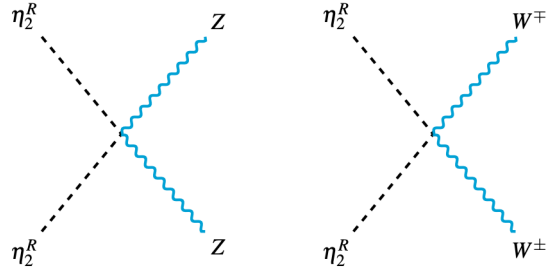


FIG. 12: Annihilation via quartic couplings for scalar DM η_2^R .

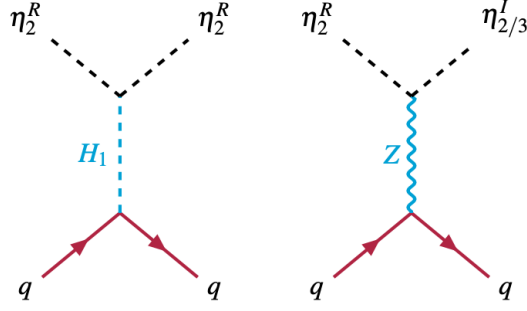


FIG. 13: Feynman diagrams of scalar DM η_2^R for the direct detection.

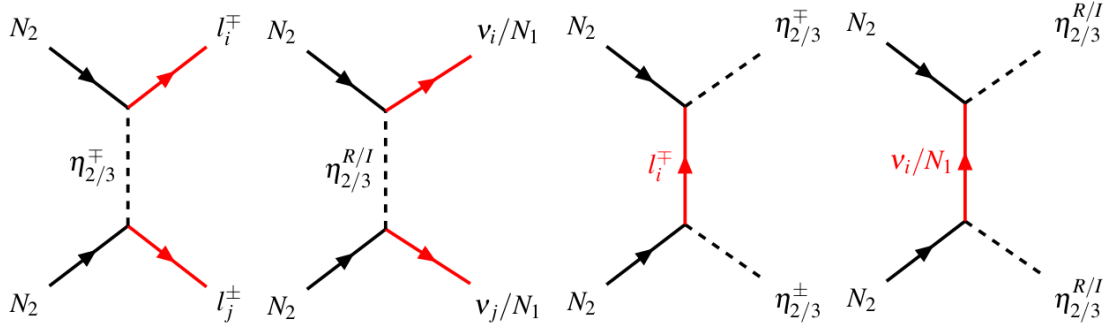


FIG. 14: Annihilation channels for fermionic DM.

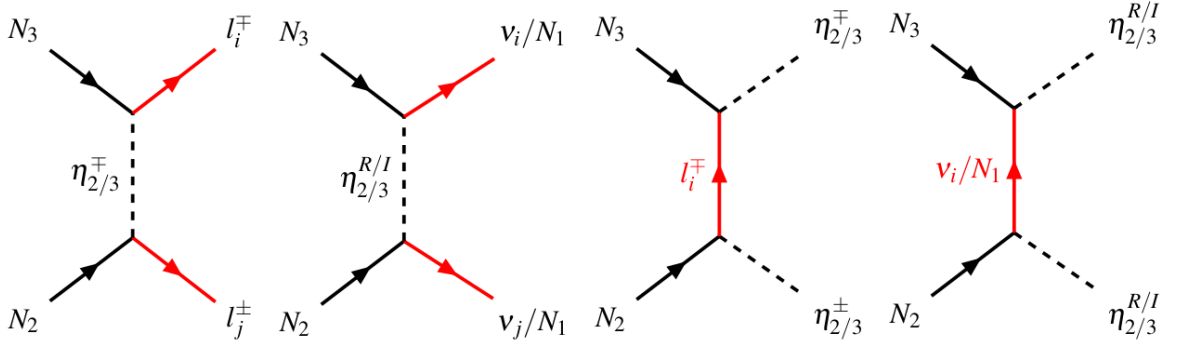


FIG. 15: Fermionic DM co-annihilation channels involving both dark fermions.

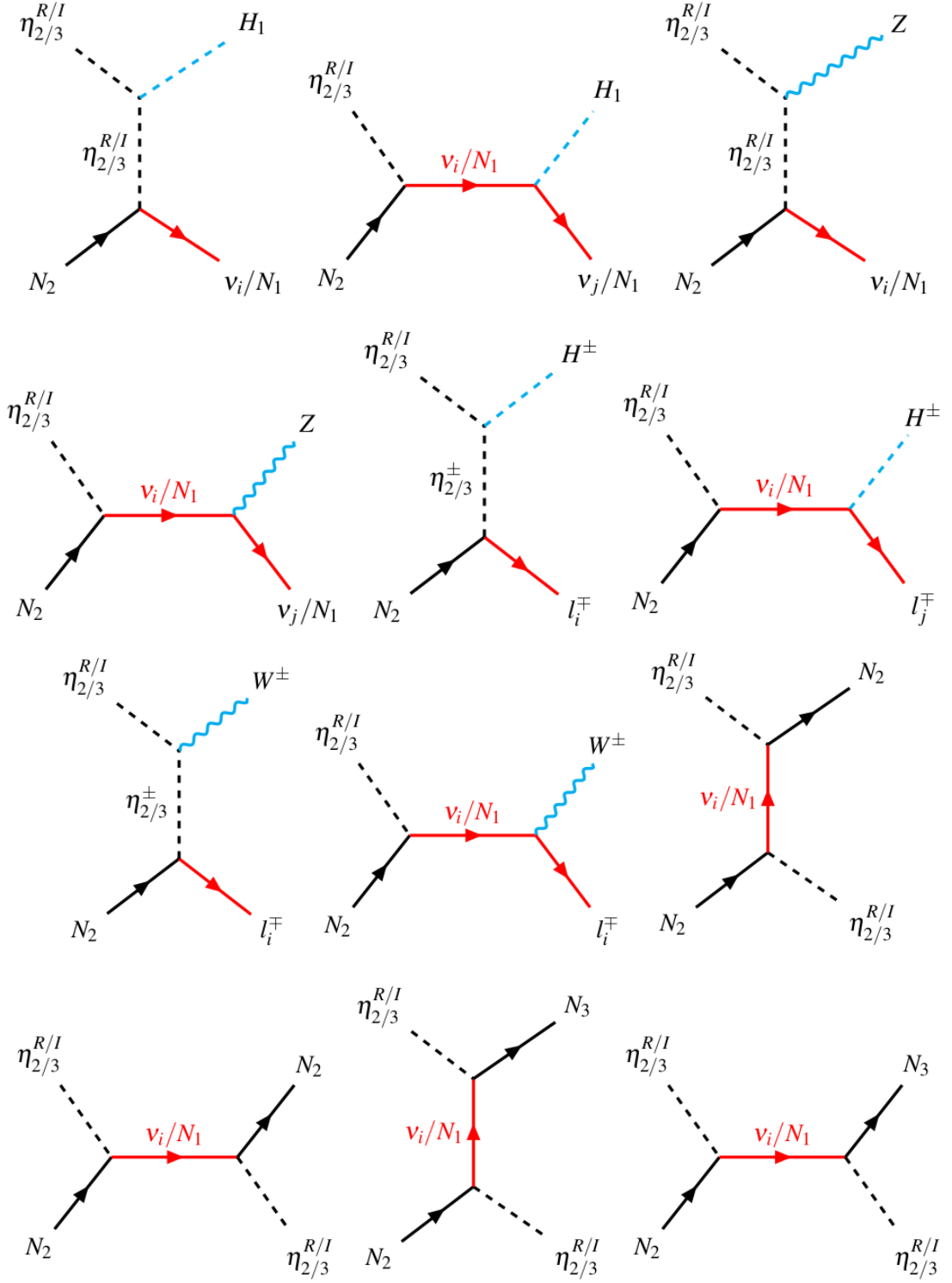


FIG. 16: Fermionic DM co-annihilation channels involving neutral dark scalars.

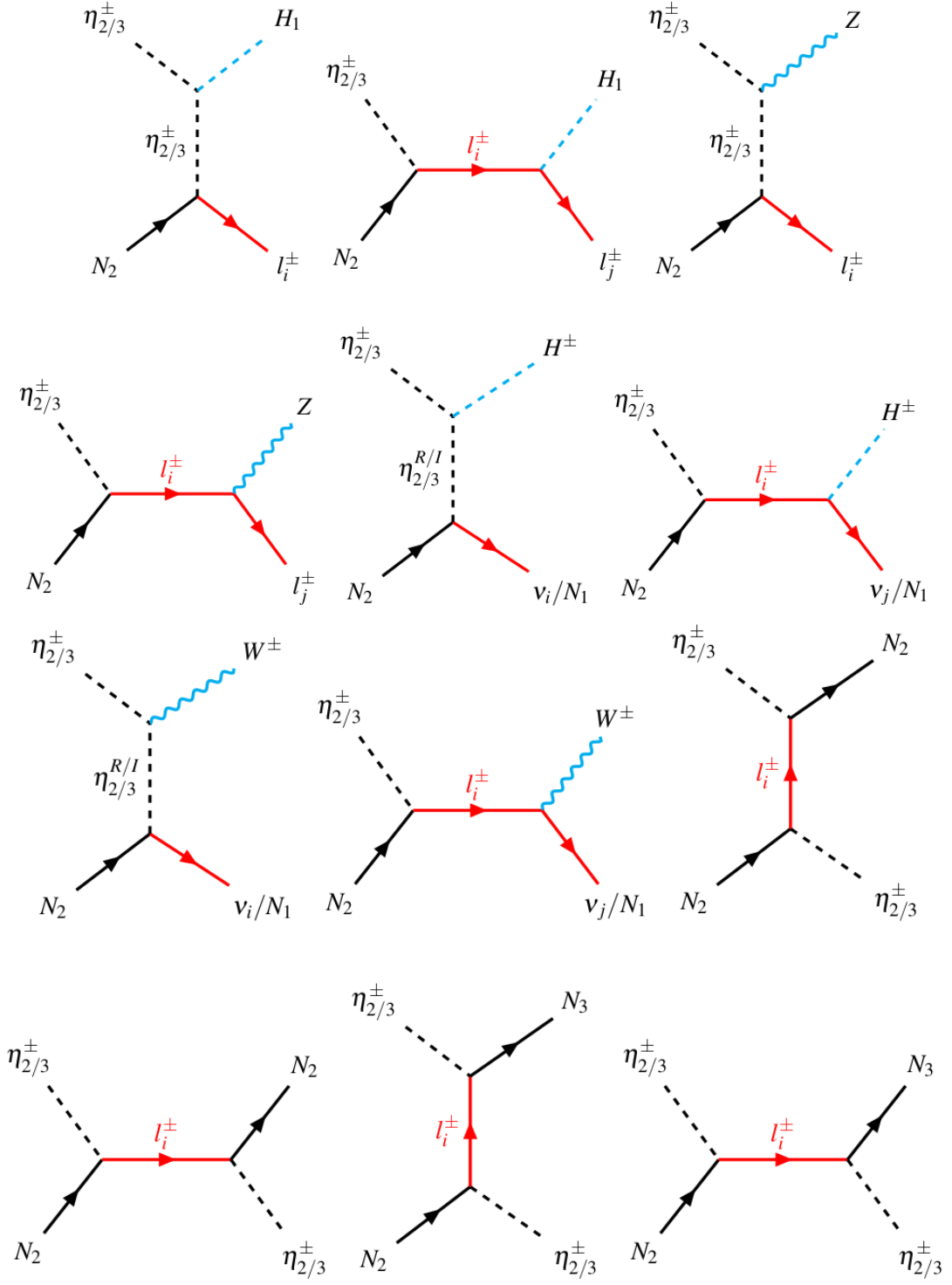


FIG. 17: Fermionic DM co-annihilation channels involving charged dark scalars.

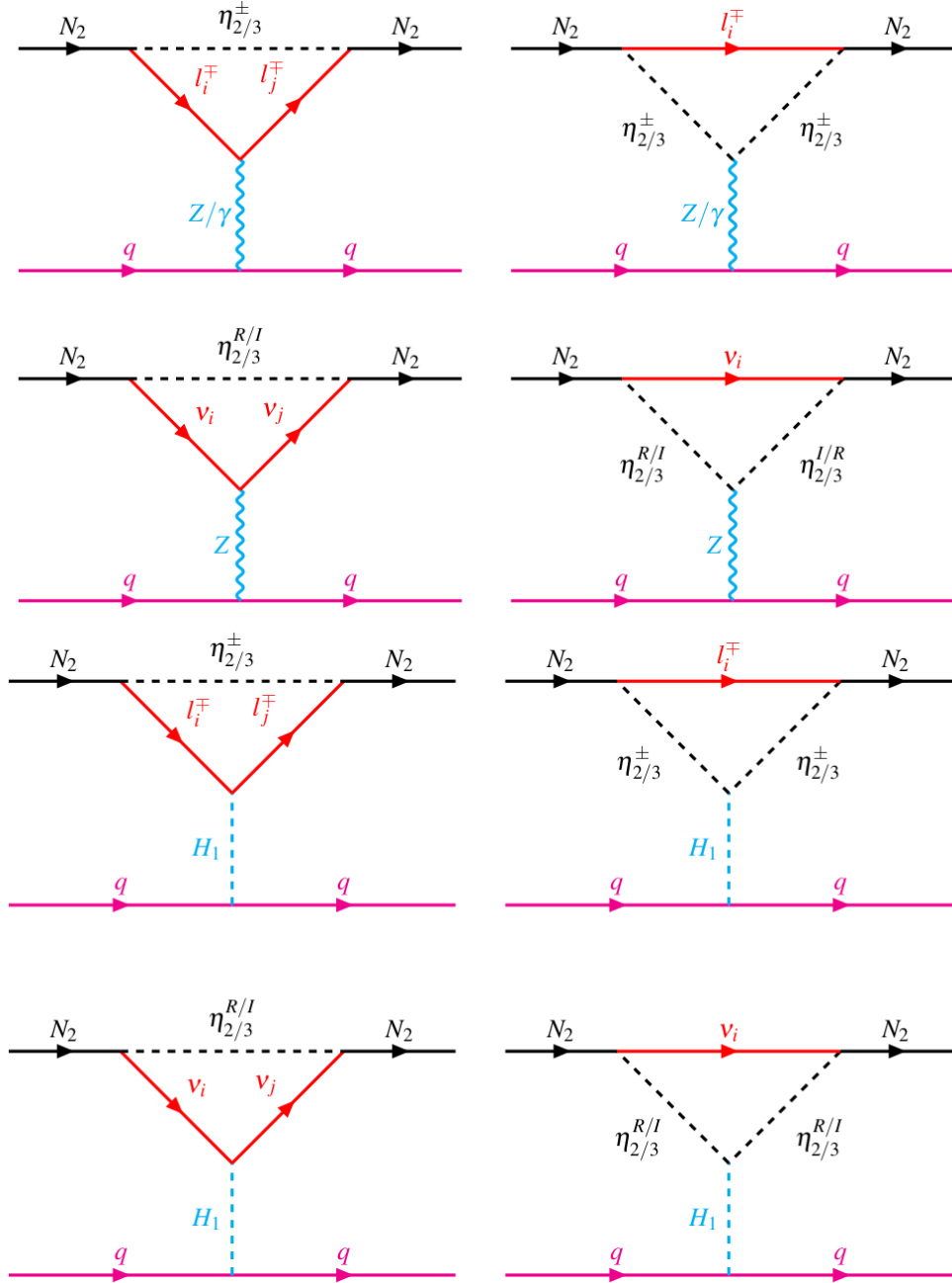


FIG. 18: Direct detection at one-loop level for fermionic DM.

-
- [1] **SNO** Collaboration, Q. R. Ahmad *et al.*, “Measurement of the rate of $\nu_e + d \rightarrow p + p + e^-$ interactions produced by ^8B solar neutrinos at the Sudbury Neutrino Observatory,” *Phys. Rev. Lett.* **87** (2001) 071301, [arXiv:nucl-ex/0106015](#).
 - [2] **Super-Kamiokande** Collaboration, Y. Fukuda *et al.*, “Evidence for oscillation of atmospheric neutrinos,” *Phys. Rev. Lett.* **81** (1998) 1562–1567, [arXiv:hep-ex/9807003](#).
 - [3] E. Ma and G. Rajasekaran, “Softly broken $A(4)$ symmetry for nearly degenerate neutrino masses,” *Phys. Rev. D* **64** (2001) 113012, [arXiv:hep-ph/0106291](#).
 - [4] K. S. Babu, E. Ma, and J. W. F. Valle, “Underlying $A(4)$ symmetry for the neutrino mass matrix and the quark mixing matrix,” *Phys. Lett. B* **552** (2003) 207–213, [arXiv:hep-ph/0206292](#).
 - [5] G. Altarelli and F. Feruglio, “Tri-bimaximal neutrino mixing, $A(4)$ and the modular symmetry,” *Nucl. Phys. B* **741** (2006) 215–235, [arXiv:hep-ph/0512103](#).
 - [6] F. Capozzi, E. Di Valentino, E. Lisi, A. Marrone, A. Melchiorri, and A. Palazzo, “Unfinished fabric of the three neutrino paradigm,” *Phys. Rev. D* **104** no. 8, (2021) 083031, [arXiv:2107.00532 \[hep-ph\]](#).
 - [7] P. F. de Salas, D. V. Forero, S. Gariazzo, P. Martínez-Miravé, O. Mena, C. A. Ternes, M. Tórtola, and J. W. F. Valle, “2020 global reassessment of the neutrino oscillation picture,” *JHEP* **02** (2021) 071, [arXiv:2006.11237 \[hep-ph\]](#).
 - [8] I. Esteban, M. C. Gonzalez-Garcia, M. Maltoni, T. Schwetz, and A. Zhou, “The fate of hints: updated global analysis of three-flavor neutrino oscillations,” *JHEP* **09** (2020) 178, [arXiv:2007.14792 \[hep-ph\]](#).
 - [9] **Planck** Collaboration, N. Aghanim *et al.*, “Planck 2018 results. VI. Cosmological parameters,” *Astron. Astrophys.* **641** (2020) A6, [arXiv:1807.06209 \[astro-ph.CO\]](#). [Erratum: *Astron. Astrophys.* 652, C4 (2021)].
 - [10] E. Ma, “Verifiable radiative seesaw mechanism of neutrino mass and dark matter,” *Phys. Rev. D* **73** (2006) 077301, [arXiv:hep-ph/0601225](#).
 - [11] E. Ma and D. Suematsu, “Fermion Triplet Dark Matter and Radiative Neutrino Mass,” *Mod. Phys. Lett. A* **24** (2009) 583–589, [arXiv:0809.0942 \[hep-ph\]](#).
 - [12] M. Hirsch, R. A. Lineros, S. Morisi, J. Palacio, N. Rojas, and J. W. F. Valle, “WIMP dark matter as radiative neutrino mass messenger,” *JHEP* **10** (2013) 149, [arXiv:1307.8134 \[hep-ph\]](#).
 - [13] A. Merle, M. Platscher, N. Rojas, J. W. F. Valle, and A. Vicente, “Consistency of WIMP Dark Matter as radiative neutrino mass messenger,” *JHEP* **07** (2016) 013, [arXiv:1603.05685 \[hep-ph\]](#).
 - [14] M. A. Díaz, N. Rojas, S. Urrutia-Quiroga, and J. W. F. Valle, “Heavy Higgs Boson Production at Colliders in the Singlet-Triplet Scotogenic Dark Matter Model,” *JHEP* **08** (2017) 017, [arXiv:1612.06569 \[hep-ph\]](#).
 - [15] S. Choubey, S. Khan, M. Mitra, and S. Mondal, “Singlet-Triplet Fermionic Dark Matter and LHC Phenomenology,” *Eur. Phys. J. C* **78** no. 4, (2018) 302, [arXiv:1711.08888 \[hep-ph\]](#).
 - [16] C. Bonilla, S. Centelles-Chuliá, R. Cepedello, E. Peinado, and R. Srivastava, “Dark matter stability and Dirac neutrinos using only Standard Model symmetries,” *Phys. Rev. D* **101** no. 3, (2020) 033011, [arXiv:1812.01599 \[hep-ph\]](#).
 - [17] S. Centelles Chuliá, R. Cepedello, E. Peinado, and R. Srivastava, “Scotogenic dark symmetry as a residual subgroup of Standard Model symmetries,” *Chin. Phys. C* **44** no. 8, (2020) 083110, [arXiv:1901.06402](#)

[hep-ph].

- [18] R. Srivastava, C. Bonilla, and E. Peinado, “The role of residual symmetries in dark matter stability and the neutrino nature,” *LHEP* **2** no. 1, (2019) 124, [arXiv:1903.01477 \[hep-ph\]](#).
- [19] S. Centelles Chuliá, R. Cepedello, E. Peinado, and R. Srivastava, “Systematic classification of two loop $d = 4$ Dirac neutrino mass models and the Diracness-dark matter stability connection,” *JHEP* **10** (2019) 093, [arXiv:1907.08630 \[hep-ph\]](#).
- [20] D. Restrepo and A. Rivera, “Phenomenological consistency of the singlet-triplet scotogenic model,” *JHEP* **04** (2020) 134, [arXiv:1907.11938 \[hep-ph\]](#).
- [21] I. M. Ávila, V. De Romeri, L. Duarte, and J. W. F. Valle, “Phenomenology of scotogenic scalar dark matter,” *Eur. Phys. J. C* **80** no. 10, (2020) 908, [arXiv:1910.08422 \[hep-ph\]](#).
- [22] S. K. Kang, O. Popov, R. Srivastava, J. W. F. Valle, and C. A. Vaquera-Araujo, “Scotogenic dark matter stability from gauged matter parity,” *Phys. Lett. B* **798** (2019) 135013, [arXiv:1902.05966 \[hep-ph\]](#).
- [23] J. Leite, O. Popov, R. Srivastava, and J. W. F. Valle, “A theory for scotogenic dark matter stabilised by residual gauge symmetry,” *Phys. Lett. B* **802** (2020) 135254, [arXiv:1909.06386 \[hep-ph\]](#).
- [24] D. Borah, R. Roshan, and A. Sil, “Minimal two-component scalar doublet dark matter with radiative neutrino mass,” *Phys. Rev. D* **100** no. 5, (2019) 055027, [arXiv:1904.04837 \[hep-ph\]](#).
- [25] A. E. Cárcamo Hernández, J. W. F. Valle, and C. A. Vaquera-Araujo, “Simple theory for scotogenic dark matter with residual matter-parity,” *Phys. Lett. B* **809** (2020) 135757, [arXiv:2006.06009 \[hep-ph\]](#).
- [26] J. Leite, A. Morales, J. W. F. Valle, and C. A. Vaquera-Araujo, “Dark matter stability from Dirac neutrinos in scotogenic 3-3-1-1 theory,” *Phys. Rev. D* **102** no. 1, (2020) 015022, [arXiv:2005.03600 \[hep-ph\]](#).
- [27] J. Leite, A. Morales, J. W. F. Valle, and C. A. Vaquera-Araujo, “Scotogenic dark matter and Dirac neutrinos from unbroken gauged B-L symmetry,” *Phys. Lett. B* **807** (2020) 135537, [arXiv:2003.02950 \[hep-ph\]](#).
- [28] N. Rojas, R. Srivastava, and J. W. F. Valle, “Simplest Scoto-Seesaw Mechanism,” *Phys. Lett. B* **789** (2019) 132–136, [arXiv:1807.11447 \[hep-ph\]](#).
- [29] D. M. Barreiros, F. R. Joaquim, R. Srivastava, and J. W. F. Valle, “Minimal scoto-seesaw mechanism with spontaneous CP violation,” *JHEP* **04** (2021) 249, [arXiv:2012.05189 \[hep-ph\]](#).
- [30] S. Mandal, R. Srivastava, and J. W. F. Valle, “The simplest scoto-seesaw model: WIMP dark matter phenomenology and Higgs vacuum stability,” *Phys. Lett. B* **819** (2021) 136458, [arXiv:2104.13401 \[hep-ph\]](#).
- [31] D. M. Barreiros, H. B. Camara, and F. R. Joaquim, “Flavour and dark matter in a scoto/type-II seesaw model,” *JHEP* **08** (2022) 030, [arXiv:2204.13605 \[hep-ph\]](#).
- [32] J. Ganguly, J. Gluza, B. Karmakar, and S. Mahapatra, “Phenomenology of the flavor symmetric scoto-seesaw model with dark matter and TM_1 mixing,” [arXiv:2311.15997 \[hep-ph\]](#).
- [33] J. Ganguly, J. Gluza, and B. Karmakar, “Common origin of θ_{13} and dark matter within the flavor symmetric scoto-seesaw framework,” *JHEP* **11** (2022) 074, [arXiv:2209.08610 \[hep-ph\]](#).
- [34] P. Van Dong and D. Van Loi, “Scotoseesaw model implied by dark right-handed neutrinos,” [arXiv:2311.09795 \[hep-ph\]](#).
- [35] J. Leite, S. Sadhukhan, and J. W. F. Valle, “Dynamical scoto-seesaw mechanism with gauged $B - L$,” [arXiv:2307.04840 \[hep-ph\]](#).

- [36] R. Kumar, P. Mishra, M. K. Behera, R. Mohanta, and R. Srivastava, “Predictions from scoto-seesaw with A_4 modular symmetry,” [arXiv:2310.02363 \[hep-ph\]](#).
- [37] W. Grimus and P. O. Ludl, “Finite flavour groups of fermions,” *J. Phys. A* **45** (2012) 233001, [arXiv:1110.6376 \[hep-ph\]](#).
- [38] R. de Adelhart Toorop, F. Feruglio, and C. Hagedorn, “Finite Modular Groups and Lepton Mixing,” *Nucl. Phys. B* **858** (2012) 437–467, [arXiv:1112.1340 \[hep-ph\]](#).
- [39] P. F. Harrison and W. G. Scott, “ μ - τ reflection symmetry in lepton mixing and neutrino oscillations,” *Phys. Lett. B* **547** (2002) 219–228, [arXiv:hep-ph/0210197](#).
- [40] P. Chen, G.-J. Ding, F. Gonzalez-Canales, and J. W. F. Valle, “Generalized $\mu - \tau$ reflection symmetry and leptonic CP violation,” *Phys. Lett. B* **753** (2016) 644–652, [arXiv:1512.01551 \[hep-ph\]](#).
- [41] M. Hirsch, S. Morisi, E. Peinado, and J. W. F. Valle, “Discrete dark matter,” *Phys. Rev. D* **82** (2010) 116003, [arXiv:1007.0871 \[hep-ph\]](#).
- [42] M. S. Boucenna, M. Hirsch, S. Morisi, E. Peinado, M. Taoso, and J. W. F. Valle, “Phenomenology of Dark Matter from A_4 Flavor Symmetry,” *JHEP* **05** (2011) 037, [arXiv:1101.2874 \[hep-ph\]](#).
- [43] L. M. G. De La Vega, R. Ferro-Hernandez, and E. Peinado, “Simple A_4 models for dark matter stability with texture zeros,” *Phys. Rev. D* **99** no. 5, (2019) 055044, [arXiv:1811.10619 \[hep-ph\]](#).
- [44] C. Bonilla, J. Herms, O. Medina, and E. Peinado, “Discrete dark matter mechanism as the source of neutrino mass scales,” *JHEP* **06** (2023) 078, [arXiv:2301.10811 \[hep-ph\]](#).
- [45] B. Grzadkowski, O. M. Ogreid, and P. Osland, “Natural Multi-Higgs Model with Dark Matter and CP Violation,” *Phys. Rev. D* **80** (2009) 055013, [arXiv:0904.2173 \[hep-ph\]](#).
- [46] N. Buskin and I. P. Ivanov, “Bounded-from-below conditions for A_4 -symmetric 3HDM,” *J. Phys. A* **54** (2021) 325401, [arXiv:2104.11428 \[hep-ph\]](#).
- [47] D. Emmanuel-Costa, O. M. Ogreid, P. Osland, and M. N. Rebelo, “Spontaneous symmetry breaking in the S_3 -symmetric scalar sector,” *JHEP* **02** (2016) 154, [arXiv:1601.04654 \[hep-ph\]](#). [Erratum: *JHEP* **08**, 169 (2016)].
- [48] **Particle Data Group** Collaboration, R. L. Workman *et al.*, “Review of Particle Physics,” *PTEP* **2022** (2022) 083C01.
- [49] S. Pramanick and A. Raychaudhuri, “Three-Higgs-doublet model under A_4 symmetry implies alignment,” *JHEP* **01** (2018) 011, [arXiv:1710.04433 \[hep-ph\]](#).
- [50] **DUNE** Collaboration, R. Acciarri *et al.*, “Long-Baseline Neutrino Facility (LBNF) and Deep Underground Neutrino Experiment (DUNE): Conceptual Design Report, Volume 2: The Physics Program for DUNE at LBNF,” [arXiv:1512.06148 \[physics.ins-det\]](#).
- [51] J. Schechter and J. W. F. Valle, “Neutrinoless Double beta Decay in $SU(2) \times U(1)$ Theories,” *Phys. Rev. D* **25** (1982) 2951.
- [52] **KamLAND-Zen** Collaboration, S. Abe *et al.*, “Search for the Majorana Nature of Neutrinos in the Inverted Mass Ordering Region with KamLAND-Zen,” *Phys. Rev. Lett.* **130** no. 5, (2023) 051801, [arXiv:2203.02139 \[hep-ex\]](#).
- [53] M. Agostini, G. Benato, and J. Detwiler, “Discovery probability of next-generation neutrinoless double- β decay experiments,” *Phys. Rev. D* **96** no. 5, (2017) 053001, [arXiv:1705.02996 \[hep-ex\]](#).
- [54] **GERDA** Collaboration, M. Agostini *et al.*, “Improved Limit on Neutrinoless Double- β Decay of ^{76}Ge from GERDA Phase II,” *Phys. Rev. Lett.* **120** no. 13, (2018) 132503, [arXiv:1803.11100 \[nucl-ex\]](#).

- [55] **CUORE** Collaboration, C. Alduino *et al.*, “First Results from CUORE: A Search for Lepton Number Violation via $0\nu\beta\beta$ Decay of ^{130}Te ,” *Phys. Rev. Lett.* **120** no. 13, (2018) 132501, [arXiv:1710.07988 \[nucl-ex\]](#).
- [56] **SNO+** Collaboration, S. Andringa *et al.*, “Current Status and Future Prospects of the SNO+ Experiment,” *Adv. High Energy Phys.* **2016** (2016) 6194250, [arXiv:1508.05759 \[physics.ins-det\]](#).
- [57] **LEGEND** Collaboration, N. Abgrall *et al.*, “The Large Enriched Germanium Experiment for Neutrinoless $\beta\beta$ Decay: LEGEND-1000 Preconceptual Design Report,” [arXiv:2107.11462 \[physics.ins-det\]](#).
- [58] **nEXO** Collaboration, J. B. Albert *et al.*, “Sensitivity and Discovery Potential of nEXO to Neutrinoless Double Beta Decay,” *Phys. Rev. C* **97** no. 6, (2018) 065503, [arXiv:1710.05075 \[nucl-ex\]](#).
- [59] **KATRIN** Collaboration, M. Aker *et al.*, “Direct neutrino-mass measurement with sub-electronvolt sensitivity,” *Nature Phys.* **18** no. 2, (2022) 160–166, [arXiv:2105.08533 \[hep-ex\]](#).
- [60] Q.-H. Cao, E. Ma, and G. Rajasekaran, “Observing the Dark Scalar Doublet and its Impact on the Standard-Model Higgs Boson at Colliders,” *Phys. Rev. D* **76** (2007) 095011, [arXiv:0708.2939 \[hep-ph\]](#).
- [61] M. Gustafsson, E. Lundstrom, L. Bergstrom, and J. Edsjo, “Significant Gamma Lines from Inert Higgs Dark Matter,” *Phys. Rev. Lett.* **99** (2007) 041301, [arXiv:astro-ph/0703512](#).
- [62] A. Pierce and J. Thaler, “Natural Dark Matter from an Unnatural Higgs Boson and New Colored Particles at the TeV Scale,” *JHEP* **08** (2007) 026, [arXiv:hep-ph/0703056](#).
- [63] **ATLAS** Collaboration, G. Aad *et al.*, “Search for invisible Higgs-boson decays in events with vector-boson fusion signatures using 139 fb^{-1} of proton-proton data recorded by the ATLAS experiment,” *JHEP* **08** (2022) 104, [arXiv:2202.07953 \[hep-ex\]](#).
- [64] **XENON** Collaboration, E. Aprile *et al.*, “First Dark Matter Search with Nuclear Recoils from the XENONnT Experiment,” *Phys. Rev. Lett.* **131** no. 4, (2023) 041003, [arXiv:2303.14729 \[hep-ex\]](#).
- [65] **LZ** Collaboration, J. Aalbers *et al.*, “First Dark Matter Search Results from the LUX-ZEPLIN (LZ) Experiment,” *Phys. Rev. Lett.* **131** no. 4, (2023) 041002, [arXiv:2207.03764 \[hep-ex\]](#).
- [66] J. Billard, L. Strigari, and E. Figueroa-Feliciano, “Implication of neutrino backgrounds on the reach of next generation dark matter direct detection experiments,” *Phys. Rev. D* **89** no. 2, (2014) 023524, [arXiv:1307.5458 \[hep-ph\]](#).
- [67] S. Antusch, J. Kersten, M. Lindner, M. Ratz, and M. A. Schmidt, “Running neutrino mass parameters in see-saw scenarios,” *JHEP* **03** (2005) 024, [arXiv:hep-ph/0501272](#).
- [68] F. Staub, “Exploring new models in all detail with SARAH,” *Adv. High Energy Phys.* **2015** (2015) 840780, [arXiv:1503.04200 \[hep-ph\]](#).
- [69] W. Porod and F. Staub, “SPHeno 3.1: Extensions including flavour, CP-phases and models beyond the MSSM,” *Comput. Phys. Commun.* **183** (2012) 2458–2469, [arXiv:1104.1573 \[hep-ph\]](#).
- [70] G. Bélanger, F. Boudjema, A. Pukhov, and A. Semenov, “micrOMEGAs4.1: two dark matter candidates,” *Comput. Phys. Commun.* **192** (2015) 322–329, [arXiv:1407.6129 \[hep-ph\]](#).
- [71] H. Ishimori, T. Kobayashi, H. Ohki, Y. Shimizu, H. Okada, and M. Tanimoto, “Non-Abelian Discrete Symmetries in Particle Physics,” *Prog. Theor. Phys. Suppl.* **183** (2010) 1–163, [arXiv:1003.3552 \[hep-th\]](#).
- [72] A. Ibarra, C. E. Yaguna, and O. Zapata, “Direct Detection of Fermion Dark Matter in the Radiative Seesaw Model,” *Phys. Rev. D* **93** no. 3, (2016) 035012, [arXiv:1601.01163 \[hep-ph\]](#).